Earth's dynamo limit of predictability controlled by magnetic dissipation

Florian Lhuillier, Julien Aubert, Gauthier Hulot

Geophysical Journal International

Geophys. J. Int. (2011) **186,** 492–508 doi: 10.1111/j.1365-246X.2011.05081.x

Earth's dynamo limit of predictability controlled by magnetic dissipation

Florian Lhuillier, Julien Aubert and Gauthier Hulot

Institut de Physique du Globe de Paris, Sorbonne Paris Cité, Université Paris Diderot, INSU/CNRS (UMR 7154*),* F-75005 *Paris, France.*
E-mail: lhuillier@ipgp.fr

Accepted 2011 May 13. Received 2011 March 16; in original form 2010 August 7

SUMMARY

To constrain the forecast horizon of geomagnetic data assimilation, it is of interest to quantify the range of predictability of the geodynamo. Following earlier work in the field of dynamic meteorology, we investigate the sensitivity of numerical dynamos to various perturbations applied to the magnetic, velocity and temperature fields. These perturbations result in some errors, which affect all fields in the same relative way, and grow at the same exponential rate $\lambda = \tau_e^{-1}$, independent of the type and the amplitude of perturbation. Errors produced by the limited resolution of numerical dynamos are also shown to produce a similar amplification, with the same exponential rate. Exploring various possible scaling laws, we demonstrate that the growth rate is mainly proportional to an advection timescale. To better understand the mechanism responsible for the error amplification, we next compare these growth rates with two other dynamo outputs which display a similar dependence on advection: the inverse τ_{SV}^{-1} of the secular-variation timescale, characterizing the secular variation of the observable field produced by these dynamos; and the inverse $(\tau_{diss}^{mag})^{-1}$ of the magnetic dissipation time, characterizing the rate at which magnetic energy is produced to compensate for Ohmic dissipation in these dynamos. The possible role of viscous dissipation is also discussed via the inverse $(\tau_{diss}^{kin})^{-1}$ of the analogous viscous dissipation time, characterizing the rate at which kinetic energy is produced to compensate for viscous dissipation. We conclude that τ_e tends to equate τ_{diss}^{mag} for dynamos operating in a turbulent regime with low enough Ekman number, and such that $\tau_{diss}^{mag} < \tau_{diss}^{kin}$. As these conditions are met in the Earth's outer core, we suggest that τ_e is controlled by magnetic dissipation, leading to a value $\tau_e = \tau_{diss}^{mag} \approx 30$ yr. We finally discuss the consequences of our results for the practical limit of predictability of the geodynamo.

Key words: Instability analysis; Non-linear differential equations; Dynamo: theories and simulations.

1 INTRODUCTION

It is now well established that the Earth's main magnetic field is generated by a dynamo operating in the liquid iron core. Since the advent of the first 3-D self-consistent dynamo simulations (Glatzmaier & Roberts 1995a,b; Kageyama *et al.* 1995), numerous dynamo models have been published and have gradually succeeded in reproducing the main properties of the geomagnetic field (Christensen & Wicht 2007). These models have led to a better understanding of the physical mechanisms at work and a better assessment of various possible approximations. In conjunction with the advent of continuous satellite measurements (Friis-Christensen *et al.* 2006; Hulot *et al.* 2007), they have recently paved the way for promising strategies of data assimilation (Fournier *et al.* 2007, 2010; Kuang *et al.* 2008). Using schemes similar to those routinely used in weather forecasting centres, they could be employed one day to improve on the current forecasts of the geomagnetic field (Maus *et al.* 2008; Beggan & Whaler 2009; Silva *et al.* 2010; Finlay *et al.* 2010). Given the non-linear nature of the equations governing the atmospheric dynamics, we know however that weather forecasts have a limited range of predictability (see Kalnay 2003). In this study we draw inspiration from pioneering work in the field of dynamic meteorology and investigate the limit of predictability that such geomagnetic forecasts would ineluctably have to face. This amounts in practice to exploring how much time in advance a geomagnetic prediction could reasonably be made.

Numerical weather forecasting progressed from an experimental to an operational procedure, thanks to the increase in computer power and an improved understanding of the physical processes that govern the atmospheric dynamics. Meteorologists quickly came to grips with the problem of the limit of weather predictability, and initially ascribed it to a combination of the insufficient knowledge of the initial conditions and the imperfect modelling of the atmospheric dynamics. It was soon recognized that the non-linear nature

of the equations governing the dynamical system was the intrinsic cause. Lorenz (1963a,b) proved that whether or not a solution can be predicted at infinite range depends on whether or not the general character of the solution was periodic. Periodic solutions are generally stable with respect to small perturbations, and can thus be forecast at infinite range. In contrast, most non-periodic solutions are very sensitive to initial conditions, meaning that two solutions originating from slightly different initial conditions may macroscopically diverge after some finite time. To investigate this issue, meteorologists proposed a dynamical approach based on the numerical integration of twin solutions with slightly different initial conditions. They measured the errors—defined as the root-mean-square (rms) differences between the two fields of wind or temperature—and studied their rate of amplification—also known as growth rate. This approach was first tested by Lorenz (1965) on a 28-variable idealized model, and next applied by Charney *et al.* (1966) to self-consistent models of atmospheric circulation then available (Smagorinsky 1963; Mintz 1964; Leith 1965). The main result was the following. No matter how small, initial errors were found to grow at some exponential rate and eventually lead to diverging predictions. Although the details of the amplification were highly dependent on several factors, it always led to an error doubling time of about five days in the early models (Charney *et al.* 1966). This value reduced to 1.5 days when investigating more recent models (Simmons *et al.* 1995). Given the current quality of meteorological data, this translates into the practical possibility of forecasting the weather up to roughly 1 week in advance (e.g. Kalnay 2003).

In this study, we focus on chaotic dynamos (a category to which the Earth's dynamo is expected to belong) in opposition to stationary dynamos [an example of which is the numerical dynamo benchmark of Christensen *et al.* (2001)]. These particular dynamos are another class of non-periodic dynamical systems, and also display a finite limit of predictability. The problems of geomagnetic and weather forecasting are indeed very similar. They rely on the numerical integration of differential equations both involving rotating convection, and have the same technical limitations—a finite number of observations in addition to finite computational resources. One important additional difficulty in the case of dynamo simulations is that they can only be run with control parameters remote from those expected for the Earth (e.g. Christensen & Wicht 2007). Too large a viscosity is for instance assumed to suppress small-scale turbulence that cannot be resolved with present computers. Two different approaches can be used to circumvent this difficulty. One is to choose combinations of values of the control parameters which lead to values of the magnetic Reynolds number compatible with those expected for the Earth. The magnetic Reynolds number describes the ratio of magnetic advection to magnetic diffusion and is a key parameter for describing the secular variation (Christensen & Tilgner 2004). The second approach involves developing scaling laws to identify the underlying physical mechanisms and then extrapolate the results from the portion of parameter space accessible to dynamo simulation to the parameter regime expected for the Earth (Christensen & Aubert 2006; Olson & Christensen 2006). Both approaches are combined in this paper.

A first study of the limit of predictability of chaotic dynamos—based on an analysis of the error growth akin to that of Lorenz (1965) and his successors—was reported in Hulot *et al.* (2010b). They introduced small errors at the initial stage of dynamo simulations and monitored the subsequent evolution of this error in several output quantities. Based on a simplified analysis of a set of simulations, they noted that the growth rate of the errors was independent of the monitored output quantity, and mainly dependent on the magnetic Reynolds number of the dynamo flow. Because the typical timescale of the magnetic secular variation displayed the same kind of dependence on the magnetic Reynolds number (Christensen & Tilgner 2004), they empirically proposed that the ratio of the error-growth timescale to the secular-variation timescale had to be roughly constant for Earth-like parameter regimes, yielding a way to evaluate the error-growth timescale for the Earth's dynamo.

In this paper, we recall the method we employ (Section 2), and extensively investigate the robustness of the error growth rate (Section 3). We then provide a detailed discussion of the mechanism responsible for this error growth (Section 4). This leads us to suggest that what likely governs the error growth rate in dynamos with Earth-like parameters is the magnetic dissipation time, characterizing the rate at which magnetic energy is produced to compensate for Ohmic dissipation. Having summarized our key results (Section 5), we conclude with some practical considerations on the limit of predictability of the geodynamo (Section 6).

2 MODELS AND TOOLS

2.1 Numerical models

We consider fluid dynamos driven by thermal convection, which operate in an electrically conducting fluid within a spherical shell $\mathcal{V}$ of aspect ratio 0.35, rotating about the z-axis with constant angular velocity Ω. The deterministic equations governing MHD and Boussinesq convection are similar to those described by Christensen & Aubert (2006), namely, the induction equation for the magnetic field $\boldsymbol{B}$ in the MHD approximation, the Navier–Stokes and heat equations for the velocity field $\boldsymbol{u}$ and the temperature field T in the Oberbeck–Boussinesq approximation. Rigid mechanical boundary conditions are employed and a constant difference of temperature ΔT between the inner and outer boundaries is considered. The outer boundary is electrically insulating, whereas the inner core is electrically conducting and free to rotate along the Earth's rotation axis. The four dimensionless control parameters of the system are the modified Rayleigh number $\mathrm{Ra}^* = \alpha g \Delta T / \Omega^2 D$ (a measure of the strength with which the dynamo is driven), the Ekman number $\mathrm{E} = \nu / \Omega D^2$ (a measure of the relative importance of viscous to Coriolis forces), the Prandtl number $\mathrm{Pr} = \nu/\kappa$ and the magnetic Prandtl number $\mathrm{Pm} = \nu/\eta$. Here, D is the shell thickness, g the gravity at the outer boundary and α the thermal expansion coefficient; ν, κ and η respectively denote the viscous, thermal and magnetic diffusivities. We use the PARODY-JA implementation of the equations (see Aubert *et al.* 2008, for details). This dynamo code, benchmarked against other major implementations (Christensen *et al.* 2001), is based on a semi-spectral method. A spherical harmonic expansion in the lateral direction is combined with a second-order finite-differencing scheme in the radial direction (with geometrical progression towards the boundaries to resolve boundary layers). As only scalar fields can be projected onto the spherical harmonic basis, the solenoidal vector fields $\boldsymbol{B}$ and $\boldsymbol{u}$ are decomposed into poloidal fields B_p and u_p, and toroidal fields B_t and u_t. Time integration involves an implicit second-order Crank–Nicholson scheme for diffusion terms and an explicit second-order Adams–Bashforth scheme for the other terms. The time steps are determined according to an adaptive criterion (see Christensen *et al.* 1999, for details).

In this study, we work with a set of 49 dynamo simulations, the features of which are summarized in Table 1. The resolutions in

Table 1. Set of numerical models. The input parameters E, Ra*, Pm, Pr are described in the main text. All simulations have been run with Pr = 1, and $t_{\rm run}$ indicates the total run time in magnetic diffusion time $\tau_\eta = D^2/\eta$. The output parameters Re (Reynolds number), Rm (magnetic Reynolds number), Ro (Rossby number), Λ (Elsasser number) are defined as $\mathrm{Re} = UD/\nu$, $\mathrm{Rm} = UD/\eta$, $\mathrm{Ro} = U/(\Omega D)$, where U is the time-averaged rms velocity over the shell $\mathcal{V}$, and $\Lambda = B^2/(\rho_0\mu_0\eta\Omega)$, where B is the time-averaged rms magnetic field, ρ_0 the fluid density and μ_0 the magnetic permeability. The dipolarity $f_{\rm dip}$ is the time-averaged rms amplitude of the dipole relative to the total field at the outer boundary. Also provided is the error growth rates $\lambda = \tau_{\rm e}^{-1}$ in units of τ_η^{-1}.

System	E	Ra*	Pm	$t_{\rm run}$	Re	Rm	Ro	Λ	Reversals?	$f_{\rm dip}$	λ
(A1)	1×10^{-2}	3	10	6	13	133	1×10^{-1}	7	No	0.35	47
(A2)	1×10^{-2}	3	20	3	13	251	1×10^{-1}	29	No	0.30	102
(A3)	1×10^{-2}	6	10	6	22	222	2×10^{-1}	23	No	0.25	119
(A4)	1×10^{-2}	6	20	3	21	428	2×10^{-1}	65	Yes	0.16	233
(A5)	1×10^{-2}	12	10	3	35	345	4×10^{-1}	44	Yes	0.18	207
(A6)	1×10^{-2}	12	20	2	33	667	3×10^{-1}	120	Yes	0.10	423
(A7)	1×10^{-2}	12	30	2	32	962	3×10^{-1}	261	Yes	0.12	623
(A8)	1×10^{-2}	24	10	2	51	509	5×10^{-1}	80	Yes	0.12	344
(A9)	1×10^{-2}	24	20	2	48	964	5×10^{-1}	265	Yes	0.10	708
(A10)	1×10^{-2}	24	30	2	47	1416	5×10^{-1}	471	Yes	0.08	1122
(B1)	1×10^{-3}	0.3	5	6	27	134	3×10^{-2}	8	No	0.55	81
(B2)	1×10^{-3}	0.3	10	3	26	255	3×10^{-2}	26	No	0.46	191
(B3)	1×10^{-3}	0.6	5	6	56	280	6×10^{-2}	2	Yes	0.17	351
(B4)	$\mathbf{1 \times 10^{-3}}$	**0.6**	**10**	**3**	**50**	**502**	$\mathbf{5 \times 10^{-2}}$	**20**	**Yes**	**0.16**	**602**
(B5)	1×10^{-3}	1.2	5	4	87	434	9×10^{-2}	12	Yes	0.08	615
(B6)	1×10^{-3}	1.2	10	2	80	803	8×10^{-2}	44	Yes	0.08	1231
(B7)	1×10^{-3}	1.2	15	2	78	1174	8×10^{-2}	78	Yes	0.07	1936
(B8)	1×10^{-3}	2.4	5	4	132	661	1×10^{-1}	28	Yes	0.07	1071
(B9)	1×10^{-3}	2.4	10	2	124	1242	1×10^{-1}	85	Yes	0.06	2196
(B10)	1×10^{-3}	2.4	15	2	121	1817	1×10^{-1}	148	Yes	0.05	3593
(C1)	3×10^{-4}	0.09	3	3	30	90	9×10^{-3}	5	No	0.83	78
(C2)	3×10^{-4}	0.09	6	2	28	170	9×10^{-3}	15	No	0.65	165
(C3)	3×10^{-4}	0.09	9	2	29	262	9×10^{-3}	27	No	0.56	258
(C4)	3×10^{-4}	0.18	3	3	63	188	2×10^{-2}	7	No	0.57	260
(C5)	3×10^{-4}	0.18	6	2	60	359	2×10^{-2}	20	No	0.44	520
(C6)	3×10^{-4}	0.18	9	2	59	529	2×10^{-2}	38	No	0.39	860
(C7)	3×10^{-4}	0.36	3	3	131	394	4×10^{-2}	3	Yes	0.14	766
(C8)	3×10^{-4}	0.36	6	2	111	667	3×10^{-2}	24	No	0.25	1386
(C9)	3×10^{-4}	0.36	9	2	107	962	3×10^{-2}	45	No	0.22	2200
(C10)	3×10^{-4}	0.72	3	3	200	599	6×10^{-2}	11	Yes	0.08	1412
(C11)	3×10^{-4}	0.72	6	2	183	1097	5×10^{-2}	38	Yes	0.08	2988
(C12)	3×10^{-4}	0.72	9	2	178	1600	5×10^{-2}	67	Yes	0.07	4683
(D1)	1×10^{-4}	0.05	1	4	58	58	6×10^{-3}	2	No	0.93	98
(D2)	1×10^{-4}	0.05	2	2	54	108	5×10^{-3}	4	No	0.87	156
(D3)	1×10^{-4}	0.1	1	3	114	114	1×10^{-2}	3	No	0.84	231
(D4)	1×10^{-4}	0.1	2	2	111	222	1×10^{-2}	8	No	0.66	447
(D5)	1×10^{-4}	0.2	1	3	278	278	3×10^{-2}	10	Yes	0.16	735
(D6)	1×10^{-4}	0.2	2	3	251	502	3×10^{-2}	4	Yes	0.13	1454
(D7)	1×10^{-4}	0.4	1	2	429	429	4×10^{-2}	3	Yes	009	1438
(D8)	1×10^{-4}	0.4	2	2	384	768	4×10^{-2}	11	Yes	0.07	2873
(D9)	1×10^{-4}	0.4	3	1	362	1086	4×10^{-2}	20	Yes	0.09	4510
(D10)	1×10^{-4}	0.8	2	1	589	1177	6×10^{-2}	23	Yes	0.05	4816
(E1)	3×10^{-5}	0.07	0.5	1.5	315	158	1×10^{-2}	2	No	0.84	619
(E2)	3×10^{-5}	0.14	0.5	1.5	663	332	2×10^{-2}	2	Yes	0.16	1957
(E3)	3×10^{-5}	0.14	1.0	1.0	668	668	2×10^{-2}	4	Yes	0.14	3662
(E4)	3×10^{-5}	0.29	0.5	1.5	1003	501	3×10^{-2}	5	Yes	0.10	3128
(E5)	3×10^{-5}	0.29	1.0	1.0	940	940	3×10^{-2}	12	Yes	0.07	5930
(F1)	1×10^{-5}	0.05	0.25	1.0	710	178	7×10^{-3}	2	No	0.85	1298
(F2)	1×10^{-5}	0.05	0.50	0.6	631	315	6×10^{-3}	5	No	0.75	1983

terms of maximum spherical harmonic degree $\ell_{\rm max}$ and number of radial grid levels $N_{\rm r}$ are selected so that at least a factor 50 may be found between the maximum energy and the energy at the cut-off wavelength in the kinetic and magnetic spectra. Depending on the simulation, this amounts in practice to varying $\ell_{\rm max}$ between 44 and 106, and $N_{\rm r}$ between 90 and 160. The Ekman number E varies from 10^{-2} to 10^{-5}, and we have chosen to explore the parameter space by alternately increasing the modified Rayleigh number Ra* and the magnetic Prandtl number Pm, keeping Pr = 1. In this way, we move from dipolar dynamos characterized by a dipolarity $f_{\rm dip} > 0.35$ to non-dipolar dynamos characterized by a dipolarity $f_{\rm dip} < 0.35$, where $f_{\rm dip}$ is the time-averaged rms amplitude of the

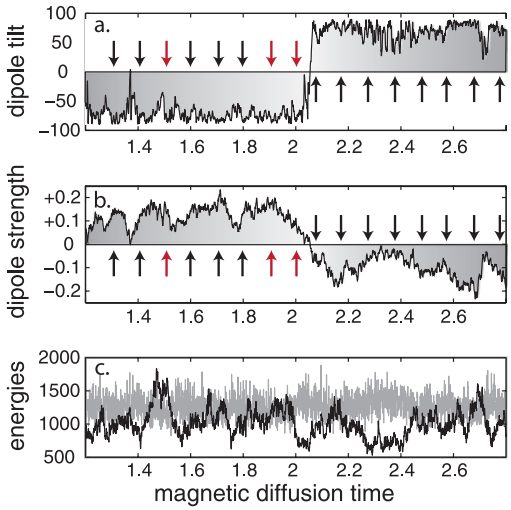

Figure 1. Reference time-series for dynamo model B4 (see Table 1 for definitions and parameters) computed with $\ell_{\max} = 44$ and $N_r = 90$: (a) dipole tilt in degrees; (b) g_1^0 axial dipole coefficient at the outer boundary in units of $(\rho_0\mu_0\eta\Omega)^{1/2}$; (c) average magnetic (black curve) and kinetic (grey curve) energy densities over the whole shell $\mathcal{V}$ in units of $\rho_0(\nu/D)^2$. The four quantities are expressed as a function of the magnetic diffusion time τ_η. The 16 arrows indicate the times when the perturbations are introduced for the cases illustrated in Fig. 2 (red) and Fig. 5 (all).

dipole relative to the total field at the outer boundary. In parallel, we also move from stable dynamos which undergo neither reversals nor significant excursions to dynamos which can reverse their polarity. The magnetic Reynolds number $\mathrm{Rm} = UD/\eta$ (where U is the time-averaged rms velocity within the dynamo shell) evolves into a range of values from 100 to 1800, which is consistent with the range of values expected for the Earth (Christensen & Tilgner 2004). We extensively investigate dynamo B4, which has the advantage of not being too expensive in terms of computational time, and consequently enables us to carry out a large number of verifications. With a magnetic Reynolds number Rm of the order of 500, it exhibits reversals but has the usual drawback of being weakly dipolar (Kutzner & Christensen 2002). A reference time-series, against which other perturbed solutions will be compared, is presented in Fig. 1. It is computed with ($\ell_{\max} = 44$, $N_r = 90$) and spans about 1.5 magnetic diffusion times. A polarity reversal occurs at around two magnetic diffusion times, whereas the polarity is globally maintained during the rest of the time. Note that all time-series will be plotted in units of magnetic diffusion time $\tau_\eta = D^2/\eta$ in the rest of the study.

2.2 Perturbative method

To investigate the growth of the errors, we first introduce various types of well-controlled perturbations in spectral space. We next monitor the departure of the perturbed solutions from the reference solution.

Type-1 perturbations refer to the simple case of radially homogeneous perturbations introduced in the axial dipole component g_1^0 of the poloidal magnetic field B_p throughout the whole shell $\mathcal{V}$. This is a natural choice because the dipole field is an important feature of the magnetic field observed outside the core. At one given step t_0 of the simulation, we thus set

$$\forall r \in \mathcal{V}, \quad \widetilde{g_1^0}(r, t_0) = g_1^0(r, t_0)\,(1 + \varepsilon)\,, \tag{1}$$

where g_1^0 is the axial dipole strength of the reference solution, $\widetilde{g_1^0}$ is the strength of the perturbed solution and ε is the amplitude of the perturbation. In this study, we rely on double precision calculations and choose amplitudes from 10^{-2} to 10^{-10}.

Type-2 perturbations are more general and correspond to introducing random perturbations in all harmonic modes y_n^m of the poloidal magnetic field B_p (type 2a), of the poloidal velocity field u_p (type 2b) or of the temperature field T (type 2c). The perturbations are still homogeneous in the radial direction but are now random in the lateral direction. At one given step t_0 of the simulation, we thus set

$$\forall r \in \mathcal{V}, \quad \widetilde{y_n^m}(r, t_0) = y_n^m(r, t_0)\left(1 + \alpha_n^m \varepsilon\right), \tag{2}$$

where the harmonic potentials y_n^m and $\widetilde{y_n^m}$ denote the reference and perturbed solutions, the α_n^m are random numbers which verify a normal law of zero mean and unit variance, and ε is the amplitude of the perturbation (varying from 10^{-2} to 10^{-10} as previously). The integers n and m denote the degrees and orders of the spherical harmonic expansion respectively. In both types 1 and 2, the perturbations are impulsive in time, meaning that the reference and perturbed fields independently evolve according to the same equations after the perturbation is introduced.

To monitor the departure of the perturbed solutions from the reference solution, we define, for any harmonic potential $y_n^m(t)$, the normalized error

$$\Delta y_n^m(r, t) = [\widetilde{y}_n^m(r, t) - y_n^m(r, t)]/\sqrt{\langle [y_n^m(r, t)]^2 \rangle}, \tag{3}$$

and in particular the axial dipole error

$$\Delta g_1^0(r, t) = [\widetilde{g}_1^0(r, t) - g_1^0(r, t)]/\sqrt{\langle [g_1^0(r, t)]^2 \rangle}, \tag{4}$$

where the angle brackets define time averaging. More generally, it will prove convenient to define a normalized rms error for any harmonic degree,

$$\Delta y_n(r, t) = \sqrt{\frac{1}{(2n+1)} \sum_{m=0}^{n} \left|\Delta y_n^m(r, t)\right|^2}, \tag{5}$$

which provides a more diagnostic view of the subsequent evolution of the errors. As we observe that the response of the dynamo system to the perturbations is large scale, it is not necessary to integrate the different errors over the whole outer shell. Rather, the rms magnetic errors—which refer to the poloidal magnetic field B_p—are evaluated at the core-mantle boundary, whereas the rms flow and temperature errors—which respectively refer to the poloidal velocity field u_p and the temperature field T—are evaluated at mid-depth of the shell.

3 ROBUSTNESS OF THE ERROR GROWTH

We start by illustrating the way any perturbation introduced in a given reference simulation results in a subsequent exponential growth of the errors in all fields (magnetic, flow and temperature). This is first shown for a case study, where we focus on the behaviour of the dipole field after an error is introduced in the axial dipole. Next, we show that a similar error growth can be found in all fields—independent of the type, the amplitude and the time of the perturbation introduced—and proceed to quantify the remarkably little variability displayed by the corresponding growth rates. Finally, we investigate the impact of the limited resolution of numerical solutions, which does not affect the estimated growth rates, but produces quantifiable errors that also grow with the same rate.

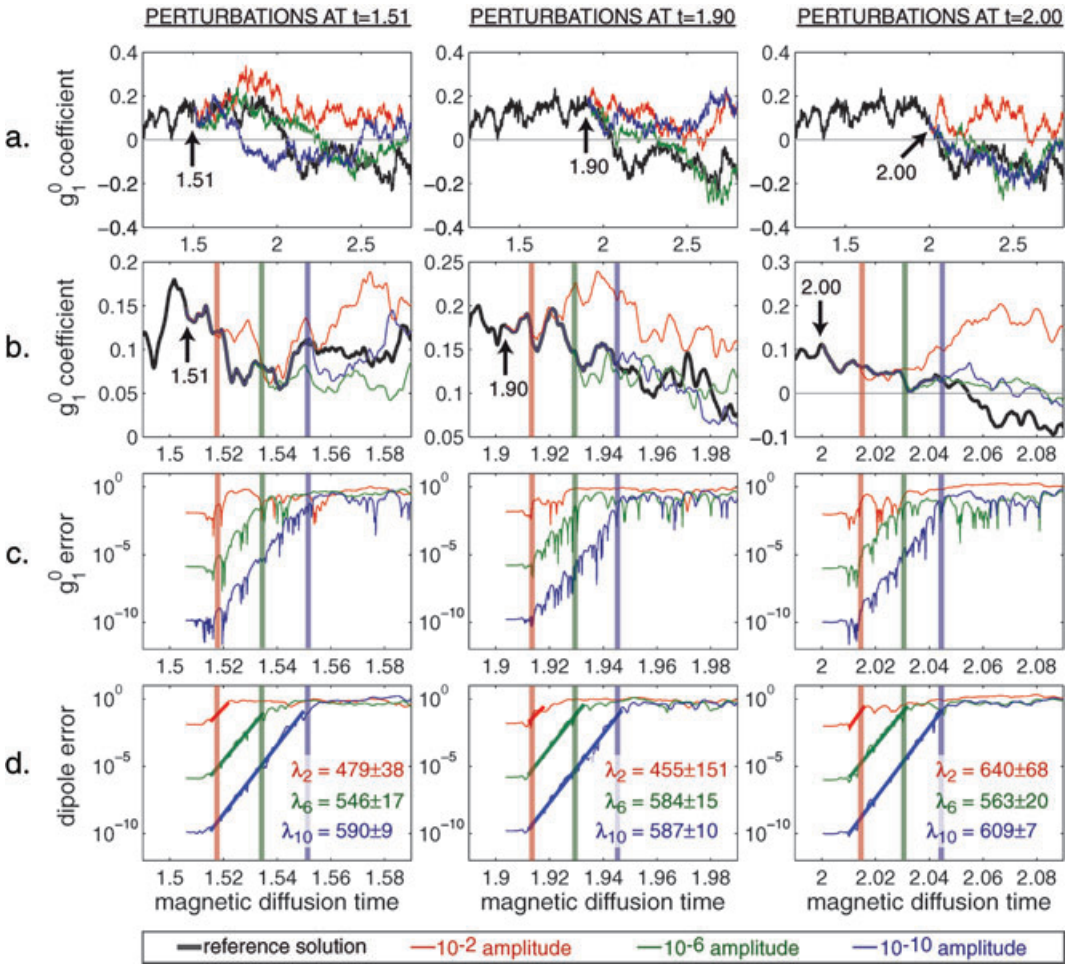

Figure 2. Consequences of introducing non-random perturbations in the g_1^0 axial dipole coefficient of dynamo B4 at three times ($t_0 = 1.51$, $t_0 = 1.9$, $t_0 = 2.0$) highlighted in red in Fig. 1. The reference time-series is represented in black, whereas the perturbed time-series are represented in red, green and blue, according to the amplitude of perturbation. The four panels show: (a) long-term evolution of the perturbed solutions; (b) short-term evolution of the perturbed solutions; (c) modulus of the axial dipole error (i.e. ln $|\Delta y_1^0|$ for the poloidal magnetic field B_p) in a semi-logarithmic plot; (d) modulus of the dipole error (i.e. ln $|\Delta y_1|$ for the poloidal magnetic field B_p) in a semi-logarithmic plot. The colour vertical lines indicate the time after which the reference and perturbed solutions drift apart in panel (b), which actually corresponds to the beginning of the free-development phase. For any of the amplitudes 10^{-2}, 10^{-6}, 10^{-10} of perturbation and any of the three times of perturbation, the exponential growth rates λ_2, λ_6 and λ_{10} of panels (d) were computed together with their uncertainty at 95 per cent confidence level (in units of τ_η^{-1}) as described in Section 3.1.

3.1 Error growth for a case study

For this case study, we focus on dynamo B4. In the reference time-series presented in Fig. 1, type-1 perturbations (computed with the help of eq. 1) were introduced at three given stages of the simulation: $t_0 = 1.51$, half a magnetic time before the reversal; $t_0 = 1.9$, at the onset of the reversal; $t_0 = 2$, when the reversal is under way. In each case, three amplitudes of perturbation were tested: 10^{-2}, 10^{-6} and 10^{-10}. Nine different perturbed solutions were thus produced, the evolutions of which are shown in Fig. 2. Fig. 2(a) details the long-term evolution of the perturbed solutions and underlines the difficulty in predicting the long-term behaviour of the perturbed solutions from the reference one. The reversal of the reference time-series may be in certain cases slightly altered, in other cases impeded, otherwise it is changed into an excursion. It is then possible to conclude that the reference and perturbed solutions evolve with no apparent relationship. In parallel with this first conclusion, Fig. 2(b) focusing on the time shortly after the introduction of the perturbation, shows that the lapse of time after which the reference and perturbed solutions drift apart depends on the amplitude of this perturbation. As could be expected, perturbed solutions separate first for the largest perturbation (10^{-2}, vertical red line), next for the medium perturbation (10^{-6}, vertical green line) and finally for the smallest perturbation (10^{-10}, vertical blue line). It is of interest that the time interval between the red and green vertical lines is approximately equal to the time interval between the green and blue vertical lines. This indicates that, every time the amplitude of the perturbation is changed by the same factor (here 10^{-4}), the same delay is introduced before the perturbed solution separates from the reference solution. This is a first clear indication of the exponential growth of the errors resulting from the perturbations.

Fig. 2(c) presents the modulus of the axial dipole error as a function of time in a semi-logarithmic scale. It demonstrates the exponential character of the error growth, and reveals three main stages in the evolution of the perturbed solutions: a mobilization phase, an exponential-growth phase and a free-development phase. The first phase, which lasts about one hundredth of magnetic time in this case, does not depend on the amplitude of the initial perturbation. It

can be interpreted as the response time of the system, during which the initial perturbation is communicated to all harmonic potentials. The second phase describes the exponential growth of the errors. As previously observed, the duration of this phase depends on the amplitude of the initial perturbation. The smaller this amplitude, the longer the duration of this phase. Note that this exponential-growth phase is much longer than the mobilization phase, which will consequently be neglected in the rest of this study. Another important feature is that the exponential growth appears to be independent of the time and amplitude of the initial perturbation, suggesting that the parameter regime investigated here is associated with a single dominant growth rate. The second phase ends when the perturbation reaches a macroscopic level which approximately corresponds to the unperturbed g_1^0 time-averaged value. Once this threshold value has been reached, the solutions then evolve with no apparent relationship to the reference solution.

We now try to quantify the dominant growth rate we identified. When $g_1^0(t)$ is perturbed with an initial amplitude ε, the averaged exponential growth can formally be written as

$$\Delta g_1^0(t) = \Delta g_1^0(0) \exp(\lambda_1^0 t), \tag{6}$$

where λ_1^0 defines the averaged growth rate. Supposing that the initial perturbation $\Delta g_1^0(0) = \varepsilon$ reaches a macroscopic level $\Delta g_1^0(\Delta t) = 1$ in a lapse of time Δt, this growth rate can then be estimated from

$$\lambda_1^0 = \frac{1}{\Delta t} \ln \left[\frac{\Delta g_1^0(0)}{\Delta g_1^0(\Delta t)} \right] = \frac{\ln(\varepsilon)}{\Delta t}. \tag{7}$$

Using this formula is however not very convenient because $\Delta g_1^0(t)$ displays some variability (recall Fig. 2c). Fortunately, analogous averaged growth rates can be defined for each harmonic mode of the poloidal magnetic field B_p and toroidal magnetic field B_t. These appear to be essentially identical and we choose to compute an estimate of their common value for each degree n of B_p, using the normalized rms errors Δy_n (eq. 5). Fig. 2(d) shows for instance the modulus of the dipole error (i.e. $|\Delta y_1|$ for the poloidal magnetic field B_p) as a function of time for the three instants and amplitudes of perturbation previously defined. The growth rate λ, which corresponds to the inverse of the e-folding time τ_e, can then be calculated using least-squares linear regression. In addition, the posterior covariance matrix can be used to quantify the uncertainty of each individual estimate of the growth rate at 95 per cent confidence level (equivalent to 2σ). Not surprisingly, this uncertainty is largest when perturbations of amplitude 10^{-2} are introduced, and the growth rate is less well recovered (Fig. 2d). For smaller perturbations, the uncertainty is however small enough and it appears that the recovered growth rates slightly fluctuate depending on the time and the amplitude of the initial perturbation. Ignoring the perturbations of amplitude 10^{-2}, the growth rates (measured in units of τ_η^{-1}) cover a restricted range of values of mean $\mu = 580$ and standard deviation $\sigma = 22$. In the following paragraph we discuss the variability of these growth rates when a larger variety of perturbations is introduced.

3.2 Variability of the error growth

We first assess the consequence of introducing other types of perturbations at a given time. For this purpose, type-2 perturbations (computed with the help of eq. 2) are introduced at $t_0 = 1.51$ in dynamo B4. The amplification of the resulting errors in the first eight degrees (i.e. for Δy_n with $n = 1$ to 8) of the various fields (magnetic, velocity and temperature) is illustrated in Fig. 3. With the same amplitudes as previously, three types of perturbations are tested: magnetic perturbations (type 2a, upper panels), flow perturbations (type 2b, middle panels) and thermal perturbations (type 2c, lower panels). Three monitoring quantities are also considered: rms magnetic errors (left column), rms flow errors (middle column) and rms temperature errors (right column). Fig. 3 shows that the mobilization phase can be seen as the time required for the magnetic, flow and temperature relative errors to become of equal amplitude. An exponential growth is then observed, regardless of the type of perturbation, the amplitude of perturbation, and the monitoring quantity. For each monitoring quantity, the growth rate and its uncertainty at 95 per cent confidence level are calculated using least-squares linear regression, by simultaneously considering the first eight Δy_n errors. The time window used to infer the growth rate is manually determined, to start after the mobilization phase and stop when the rms error reaches a macroscopic level. This growth rate displays a slight variability, depending on the type of perturbation, the amplitude of perturbation and the monitoring quantity.

To better quantify this variability, we chose to investigate numerous cases when magnetic perturbations were applied. For each of the five considered amplitudes (10^{-2}, 10^{-4}, 10^{-6}, 10^{-8} and 10^{-10}), 100 random perturbations were introduced (still at time $t_0 = 1.51$ in dynamo B4). Histograms of the magnetic, kinematic and thermal growth rates (again computed by simultaneously considering the errors in the first eight degrees of the monitoring quantity) are presented in Fig. 4, where values were collected in bins with width comparable to the 95 per cent confidence level with which each individual estimate was recovered. These plots again confirm that individual estimates are recovered with sufficient accuracy that, for each observed quantity, the intrinsic variability of the growth rate with respect to the perturbation introduced can be assessed. This variability can be quantified by fitting each histogram with a normal distribution, providing estimates of the mean μ and standard deviation σ. This standard deviation does not exceed 6 per cent of the mean value. Disregarding the perturbations of amplitude 10^{-2} as previously, a standard deviation of less than 3 per cent is found between the histograms, which confirms that the growth rates are not significantly different. The exponential growth is slightly slower for the perturbations of amplitude 10^{-2} but this behaviour may be justified by the fact that the system rapidly saturates and does not have the time to produce a regular exponential growth.

To finally assess the variability of the growth rate as a function of the time of perturbation, magnetic, flow and temperature perturbations of amplitude 10^{-10} were introduced in dynamo B4 at each of the different times highlighted in Fig. 1. The values of the magnetic, kinematic and thermal growth rates (computed in the same manner) are plotted in Fig. 5. At any given time, the growth rate is fairly independent of the perturbation introduced and the monitoring quantity, with a standard deviation of the order of 3 per cent in the present case. The main source of variability thus stems from the time of the perturbation, with a standard deviation of the order of 6 per cent in this case. No correlation has been found between the growth rate and the magnetic or kinetic energies.

To sum up, the variability of the growth rate is the result of two main contributions: (1) a temporal variability of the order of 6 per cent, depending on the time the perturbation is introduced but uncorrelated with macroscopic energies; (2) an intrinsic variability generally of the order of 3 per cent due to the introduction of random perturbations at the initial time. Type and amplitude of perturbation are not determining factors, except for the case when the amplitude is strong and the system saturates. The variations of the growth rate are at any rate limited and do not contradict the idea that the growth rate represents a general feature of the dynamo mean state. We thus

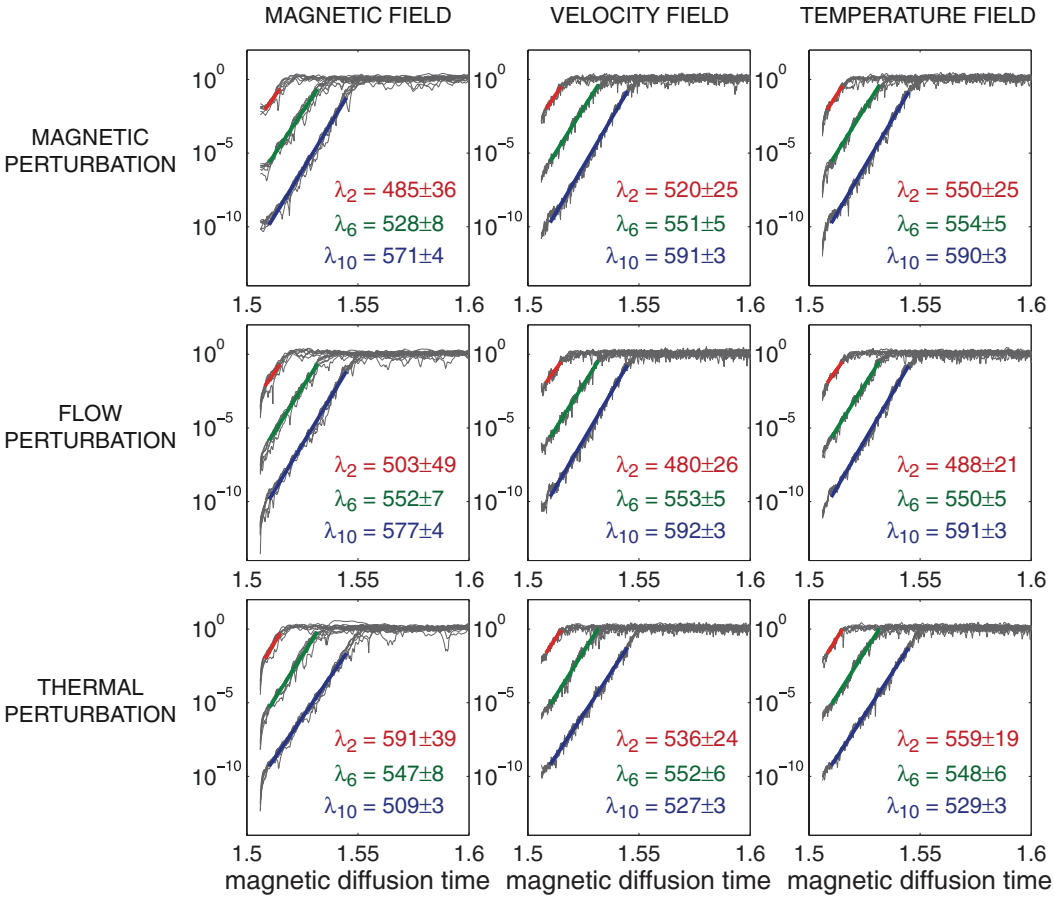

Figure 3. Consequences of introducing random perturbations in dynamo B4 at $t_0 = 1.51$. The first line corresponds to magnetic perturbations (type 2a), the second line to flow perturbations (type 2b) and the third line to thermal perturbations (type 2c) at the initial time. The first column represents magnetic errors, the second column flow errors and the third column thermal errors, as defined by the normalized rms errors $\Delta y_n(t)$ and plotted for $n = 1$ to 8. Three amplitudes of perturbation were tested : 10^{-2} in red, 10^{-6} in green, 10^{-10} in blue. The exponential growth rates λ_i are determined using least-squares linear regression, simultaneously over the first eight Δy_n errors. They are as previously estimated with a confidence level of 95 per cent.

conclude that a characteristic growth rate can be determined for each dynamo simulation.

For all the results discussed in Section 4, growth rates are computed in the following way. For each dynamo solution, magnetic random perturbations of amplitude 10^{-10} are introduced at 10 different times over a period of at least one magnetic diffusion time. Magnetic random perturbations have been arbitrarily chosen, because the three types of perturbation lead to the same growth rate; and weak amplitudes of perturbation have been favoured, because they lead to more accurate estimates of the slope. Growth rates are next jointly determined over the first eight harmonic degrees of the magnetic errors for each of the 10 perturbation times, with the same procedure as previously described. The corresponding 10 estimates are finally used to obtain an averaged growth rate λ together with its uncertainty at 95 per cent confidence level. The corresponding values of λ and its associated $\tau_e = \lambda^{-1}$ are provided in Table 1.

3.3 Impact of limited resolution

Instead of introducing initial perturbations of known amplitude, we now wish to explore the impact of limited spatial resolution. To illustrate this point, we rely on dynamo B4 with a higher angular spatial resolution than previously ($\ell_{\max} = 128$ instead of $\ell_{\max} = 44$). Fig. 6(a) presents the dipole tilt associated with this extended reference time-series, and Fig. 6(b) its magnetic spectrum integrated over the whole shell $\mathcal{V}$.

In a first series of tests we removed the energy in the small scales of the magnetic field (both poloidal and toroidal) by setting to zero all spherical harmonic degrees beyond a given degree $\ell_{\rm tr}$, at a given time step t_0. The reset solution is next left free to evolve with the same resolution as the extended reference time-series. These tests were carried out for four different times t_0 (Fig. 6a), and four different truncation degrees ($\ell_{\rm tr} = 44$, 96, 112 and 120). As illustrated in Fig. 7(a) for the poloidal magnetic field when the reset takes place at time $t_0 = 10.505$, the rms errors Δy_n (computed from eq. 5) exponentially grow. The growth rates (calculated by least-squares linear regression, by simultaneously considering the first eight Δy_n) are moreover consistent with those previously inferred for dynamo B4 (within the variability already discussed in Section 3.2). This underlines the generality of the error growth mechanism, and indicates that its value does not significantly depend on the spatial resolution of the simulations.

To assess more directly the impact of limited spatial resolution in numerical simulations, we carried out a second series of tests. We permanently set to zero all spherical harmonic degrees of all fields (magnetic, flow and temperature) beyond a given degree $\ell_{\rm tr}$, starting at a given time step t_0. As illustrated in Fig. 7(b) for the poloidal magnetic field when the change in resolution takes place

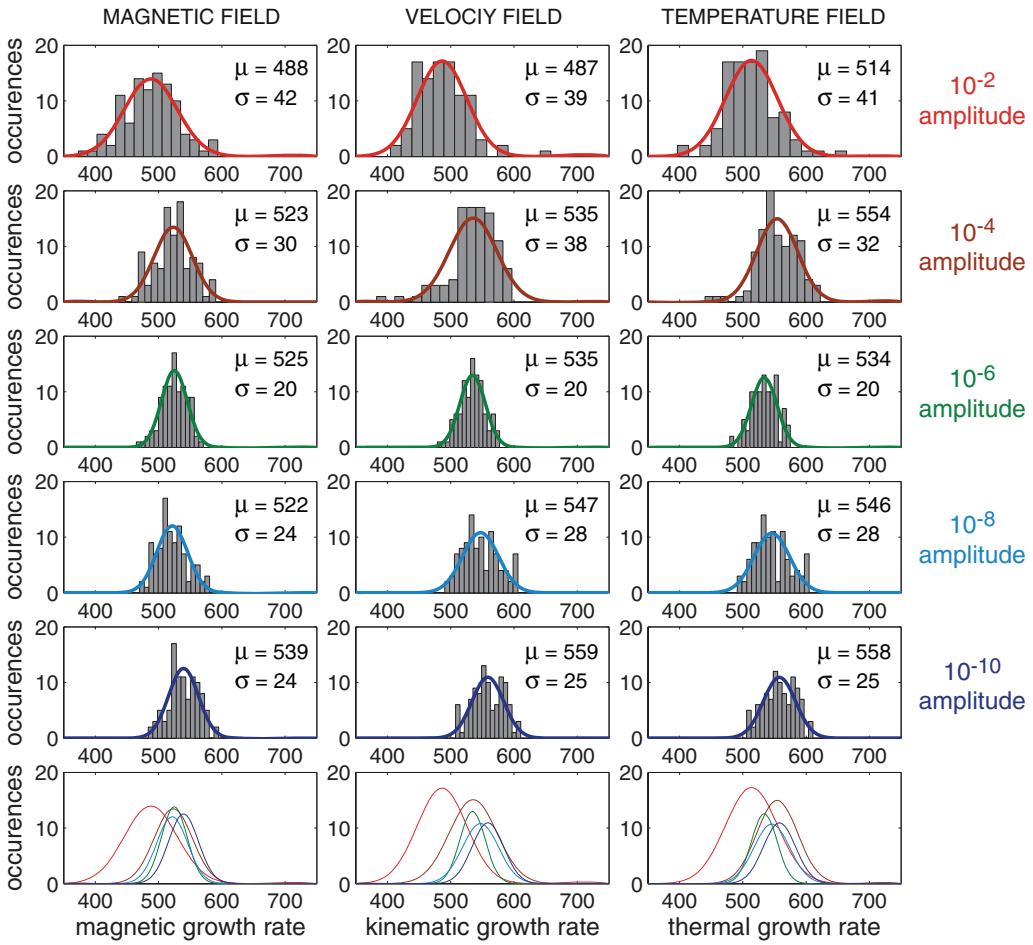

Figure 4. Histograms of the magnetic (column 1), kinematic (column 2) and thermal (column 3) growth rates for magnetic perturbations introduced in dynamo B4 at time $t_0 = 1.51$. The histograms are modelled by normal distributions, the mean μ and standard deviation σ of which are indicated on the right of each panel (in units of τ_η^{-1}). The first five lines show histograms for amplitudes of perturbation from 10^{-2} to 10^{-10}. The sixth line is a summary of the results.

from time t_0, we found again that the rms errors Δy_n (computed from eq. 5) exponentially grow, and that the recovered growth rates are consistent with those previously inferred for dynamo B4. It thus appears that two dynamo solutions, starting from the same initial state but only contrasting by their level of resolution, will differ by an error growing exponentially with the same growth rate as an error resulting from an initial seed perturbation introduced in either of the two solutions.

As shown in Fig. 7(b), the error is larger when the level of resolution is lower. To quantify this trend, we plotted in Fig. 8 the equivalent magnetic perturbation (i.e. the amplitude at which the rms errors Δy_n begin to grow after the brief mobilisation phase in Fig. 7b) as a function of the loss of magnetic energy due to the non-modelled small scales (i.e. the ratio of the truncated tail of the magnetic spectrum to the entire magnetic spectrum, see Figs 6b and c). It suggests that the non-modelled magnetic energy can provide a rough measure of the equivalent magnetic perturbation. Note however that the best-fitting trend in this log–log plot reveals that the equivalent magnetic perturbation is intermediate between being proportional to the relative missing magnetic energy and its square root, which probably comes from the role played by the missing small-scale flow and thermal fields in defining the equivalent magnetic perturbation. In this respect, Fig. 8 should not be over-interpreted. It simply suggests that estimating the relative contribution of the non-modelled magnetic energy is able to provide an order of magnitude of an equivalent magnetic perturbation, which in turn can be used to assess the limit of predictability of a simulation with a given limited spatial resolution.

By analogy with the issue of limited spatial resolution, the impact of limited temporal resolution in numerical simulations can also be assessed. To this end, we still relied on dynamo B4 and produced two solutions with fixed time-steps (contrary to the previous ones produced with an adaptive time-step varying between 1×10^{-6} and 5×10^{-6} τ_η): one well-resolved with a time-step of $\Delta t = 10^{-8}$ τ_η, one of lesser resolution computed starting from the previous solution at a given time t_0 but with a time-step of $\Delta t = 10^{-6}$ τ_η from there on. As illustrated in Fig. 9, the rms errors Δy_n between these two solutions after t_0 (computed according to eq. 5) led to an exponential growth, the rate of which was found to be consistent with those previously inferred for dynamo B4. Note that the equivalent magnetic perturbation (i.e. the amplitude at which the rms errors Δy_n begin to grow after the brief mobilization phase in Fig. 9) is now of the order of 10^{-5} for a decrease of two orders of magnitude in the time-step. It thus suggests that the impact of limited temporal resolution is by far less acute than the impact of limited spatial resolution, which appears to be the main

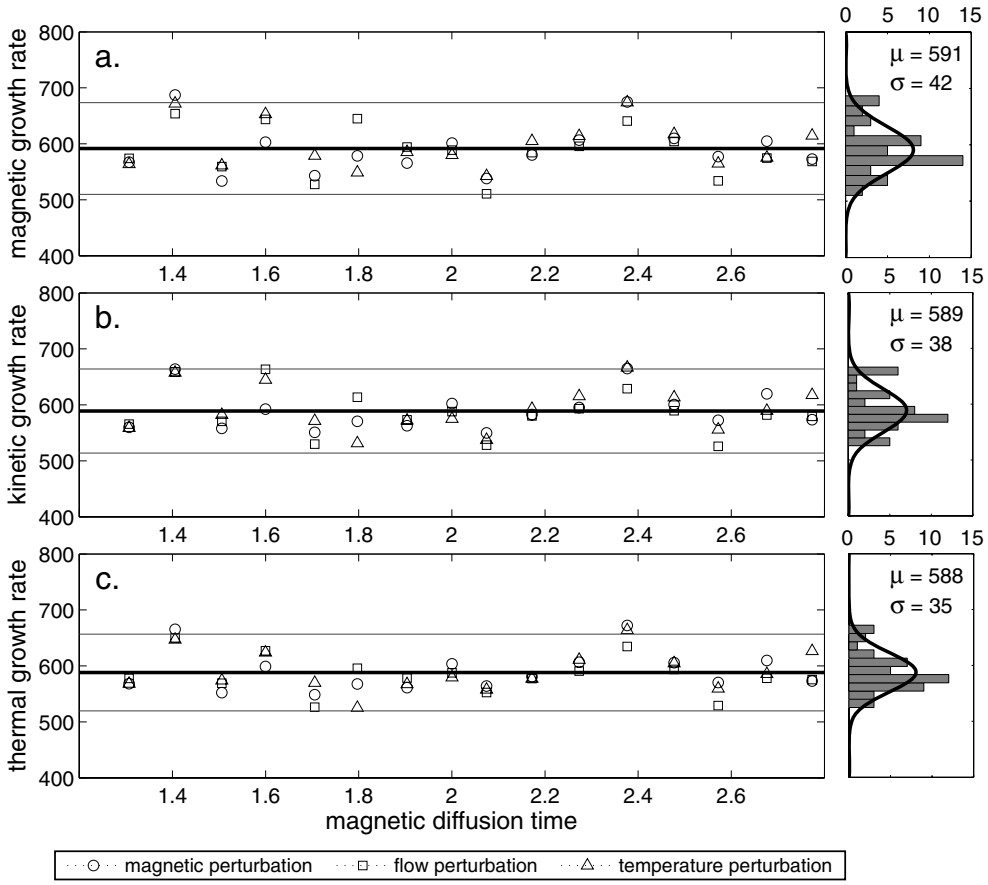

Figure 5. Variability of the growth rate as a function of time for dynamo B4. Random perturbations of amplitude 10^{-10} were introduced at the 16 times highlighted in Fig. 1. Magnetic, flow and temperature perturbations were alternately tested. The three panels depict: (a) the magnetic growth rates; (b) the kinematic growth rates and (c) the thermal growth rates. The histograms on the right show the distribution of the growth rates, irrespective of the type of perturbation. They can be modelled by normal distributions, the mean μ and standard deviation σ of which are indicated on the right of each panel (in units of τ_η^{-1}).

source of error associated with the limited resolution of numerical simulations.

4 SCALING LAWS

4.1 Cause of the error growth

We now wish to investigate the cause of the observed error growth. Let us denote ($\boldsymbol{B}_0$, $\boldsymbol{u}_0$, T_0, P_0) the reference solution and ($\boldsymbol{B}_0+\boldsymbol{B}$, $\boldsymbol{u}_0+\boldsymbol{u}$, T_0+T, P_0+P) the perturbed solution after the mobilization phase. Both solutions are dynamo solutions and thus satisfy the equations governing MHD and Boussinesq convection (e.g. Christensen & Aubert 2006), that is, for the reference state

$$\frac{\partial \boldsymbol{u}_0}{\partial t}+(\boldsymbol{u}_0\cdot\nabla)\,\boldsymbol{u}_0=-\frac{1}{\rho_0}\nabla P_0+\nu\Delta\boldsymbol{u}_0+\alpha T_0\boldsymbol{g}-2\boldsymbol{\Omega}\times\boldsymbol{u}_0 +\frac{1}{\mu_0\rho_0}(\nabla\times\boldsymbol{B}_0)\times\boldsymbol{B}_0; \tag{8}$$

$$\frac{\partial T_0}{\partial t}+(\boldsymbol{u}_0\cdot\nabla)\,T_0=\kappa\Delta T_0; \tag{9}$$

$$\frac{\partial \boldsymbol{B}_0}{\partial t}=\nabla\times(\boldsymbol{u}_0\times\boldsymbol{B}_0)+\eta\Delta\boldsymbol{B}_0, \tag{10}$$

where ρ_0 is the density of the core and μ_0 is the magnetic permeability.

Assuming the perturbations to be small and linearizing about the reference state then yields the following three equations:

$$\frac{\partial \boldsymbol{u}}{\partial t}+\underbrace{(\boldsymbol{u}_0\cdot\nabla)\,\boldsymbol{u}}_{(i)}+\underbrace{(\boldsymbol{u}\cdot\nabla)\,\boldsymbol{u}_0}_{(ii)}=-\frac{1}{\rho_0}\nabla P+\nu\Delta\boldsymbol{u}+\alpha T\boldsymbol{g}-2\boldsymbol{\Omega}\times\boldsymbol{u} +\frac{1}{\mu_0\rho_0}[(\nabla\times\boldsymbol{B})\times\boldsymbol{B}_0+(\nabla\times\boldsymbol{B}_0)\times\boldsymbol{B}]; \tag{11}$$

$$\frac{\partial T}{\partial t}+\underbrace{(\boldsymbol{u}_0\cdot\nabla)\,T}_{(i)}+\underbrace{(\boldsymbol{u}\cdot\nabla)\,T_0}_{(iii)}=\kappa\Delta T; \tag{12}$$

$$\frac{\partial \boldsymbol{B}}{\partial t}=\underbrace{\nabla\times(\boldsymbol{u}_0\times\boldsymbol{B})}_{(i)}+\underbrace{\nabla\times(\boldsymbol{u}\times\boldsymbol{B}_0)}_{(iv)}+\eta\Delta\boldsymbol{B}. \tag{13}$$

which respectively describe the evolution of the flow, temperature and magnetic perturbations. All those equations display at least one term [labelled (i) in each equation] that can produce some exponential growth of $\boldsymbol{u}$, T and $\boldsymbol{B}$. A first-order dimensional analysis of those terms immediately suggests a possible growth rate scaling as $\lambda\propto U_0/D$. (Note that for the purpose of the present discussion, all dynamo output quantities such as U_0 with a 0 index

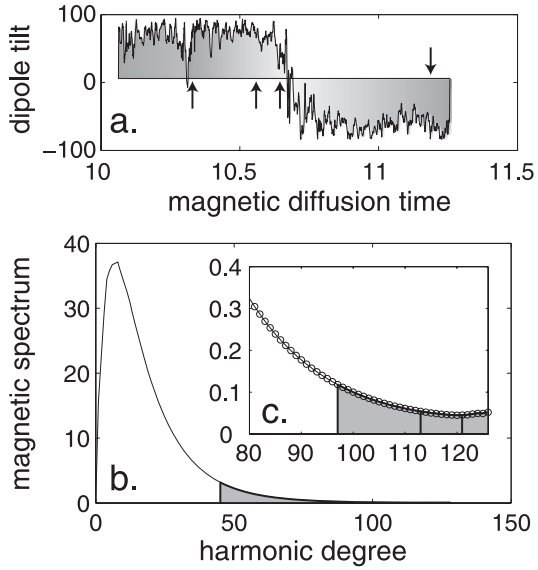

Figure 6. Extended reference time-series for dynamo B4 (Table 1) computed with $\ell_{max} = 128$ and $N_r = 96$: (a) dipole tilt in degrees; (b) magnetic spectrum integrated over the whole shell $\mathcal{V}$ (in units of $\rho_0\mu_0\eta\Omega$) and (c) enlargement of the spectrum tail. Arrows in panel (a) indicate times when tests are applied, whereas the vertical black lines in panels (b) and (c) correspond to the various values of ℓ_{tr} (44, 96, 112 and 120) considered in our tests.

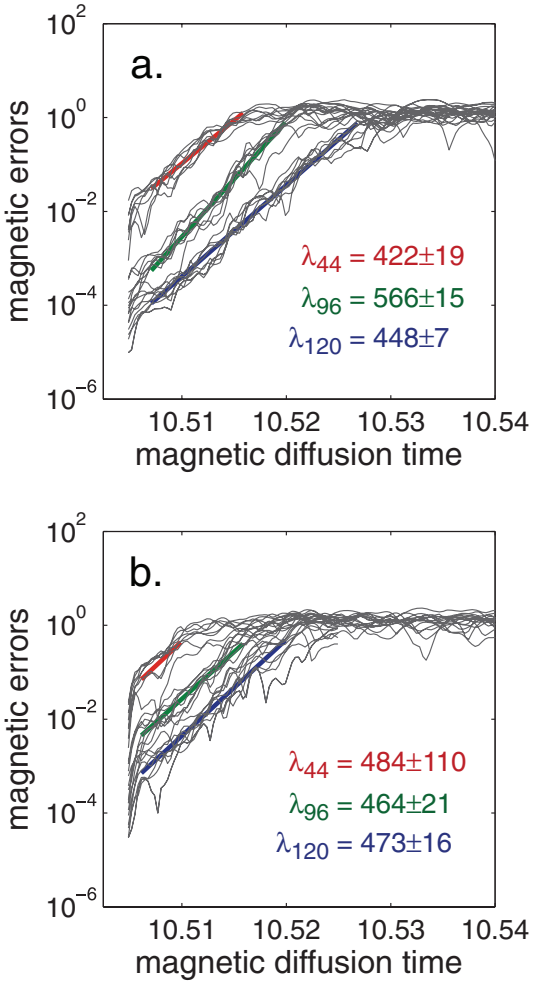

Figure 7. Impact of limited spatial resolution in dynamo B4: (a) magnetic error growth (as measured by the normalized poloidal field rms errors Δy_n for n = 1–8) after setting to zero all spherical harmonic degrees of the magnetic field (both poloidal and toroidal) beyond degrees ℓ_{tr} in the extended reference time-series of Fig. 6(a), at time step $t_0 = 10.505$; (b) magnetic error growth [measured as in (a)] after permanently setting to zero all spherical harmonic degrees of all fields (magnetic, flow and temperature) beyond degrees ℓ_{tr} in the extended reference time-series, from time step $t_0 = 10.505$. In both (a) and (b), three values of ℓ_{tr} (44, red; 96, green; and 120, blue) were shown and the growth rates (in units of τ_η^{-1}) were estimated with their uncertainties at 95 per cent confidence level.

will relate to the unperturbed dynamo solution, whereas analogous quantities without any index will refer to the perturbation) However, those equations also display diffusive terms ($\nu\Delta\boldsymbol{u}$ in eq. 11, $\kappa\Delta T$ in eq. 12 and $\eta\Delta\boldsymbol{B}$ in eq. 13), and a number of terms coupling the flow ($\boldsymbol{u}$), temperature (T) and magnetic ($\boldsymbol{B}$) perturbations. Some of those terms, labelled (ii), (iii) and (iv) are quite similar in form as the (i)-terms. As noted in Section 3.2, the mobilization phase can be seen as the time required to produce the equilibrium $U/U_0 = T/T_0 = B/B_0$ (presumably via a balance between the buoyancy, Coriolis and Lorentz terms in eqs 8 and 11). In these conditions, the (ii)–(iv) terms respectively scales as $\frac{U_0 U}{D}, \frac{U T_0}{D} = \frac{U}{U_0}\frac{T_0}{T}\frac{U_0 T}{D} = \frac{U_0 T}{D}, \frac{U B_0}{D} = \frac{U}{U_0}\frac{B_0}{B}\frac{U_0 B}{D} = \frac{U_0 B}{D}$. In a regime where advection renders the various diffusive terms of secondary importance, we thus obtain that the natural scaling for the error growth rate we observe is $\lambda \propto U_0/D$.

Depending on which timescale one uses, this scaling law can then be written as $\lambda\tau_\eta \propto (U_0 D)/\eta = \mathrm{Rm}$ (the magnetic Reynolds number) if using the magnetic diffusion time $\tau_\eta = D^2/\eta$, $\lambda\,\tau_\kappa \propto (U_0 D)/\kappa = \mathrm{Pe}$ (the Péclet number) if using the thermal diffusion time $\tau_\kappa = D^2/\kappa$, $\lambda\tau_\nu \propto (U_0 D)/\nu = \mathrm{Re}$ (the Reynolds number) if using the kinematic diffusion time $\tau_\nu = D^2/\nu$, and $\lambda\Omega^{-1} \propto U_0/(\Omega D) = \mathrm{Ro}$ (the Rossby number) if using the inverse rotation frequency Ω^{-1}. In principle, if λ indeed only scales like U_0/D, any of the four timescales $\tau = \{\tau_\eta, \tau_\kappa, \tau_\nu, \Omega^{-1}\}$ should lead $\lambda\tau$ to plot as a linear function of the corresponding Rm, Pe, Re or Ro number. Yet, this is not the case. This can be seen in Fig. 10, which shows only three such plots, because all our simulations were run with $\mathrm{Pr} = 1$, leading to $\mathrm{Pe} = \mathrm{Re}$ and $\tau_\kappa = \tau_\nu$ so that plotting $\lambda\tau_\kappa$ as a function of Pe would be exactly the same as plotting $\lambda\tau_\nu$ as a function of Re.

Fig. 10(a) which shows $\lambda\tau_\eta$ as a function of Rm, indeed suggests that λ in units of τ_η^{-1} is proportional to Rm. But it also shows that the factor of proportionality is sensitive to the Ekman number E. This sensitivity was attributed by Hulot *et al.* (2010b) to a geometrical effect of the leading scales of the background dynamo flows. Plotting $\lambda\tau_\nu$ as a function of Re provides a complementary perspective (Fig. 10b). This figure can be seen as a transform of Fig. 10a via the common multiplication of both abscissa and ordinate of each point by the magnetic Prandtl number Pm. As Pm-values in our simulations are roughly related to E-values (recall Table 1), with larger values of Pm being associated with larger values of E, this leads to a reorganisation of the various segments of Fig. 10(a) into a mainly piecewise succession of segments in Fig. 10(b). Runs with various Pm values were nevertheless computed for each E, and this also reveals some sensitivity of λ with respect to Pm, as is best seen in Fig. 10(c), which now shows $\lambda\Omega^{-1}$ as a function of Ro. The advantage of such a plot is that both abscissa and ordinates no longer refer to any of the diffusive parameters η and ν, so that the sensitivity of λ to those parameters (via E and Pm) are directly to be found in the behaviour of the plot itself. This plot shows that $\lambda\Omega^{-1}$ is proportional to Ro, with a slope that depends on E, but also

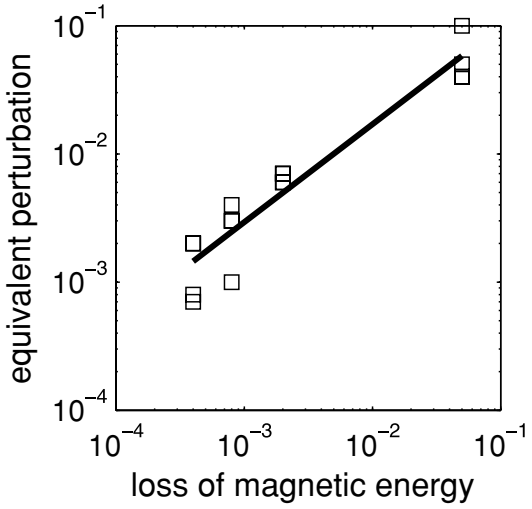

Figure 8. Log–log plot of the equivalent magnetic perturbation as a function of the relative contribution of the non-modelled small-scale magnetic field to the total magnetic field energy over the entire core (see text for details).

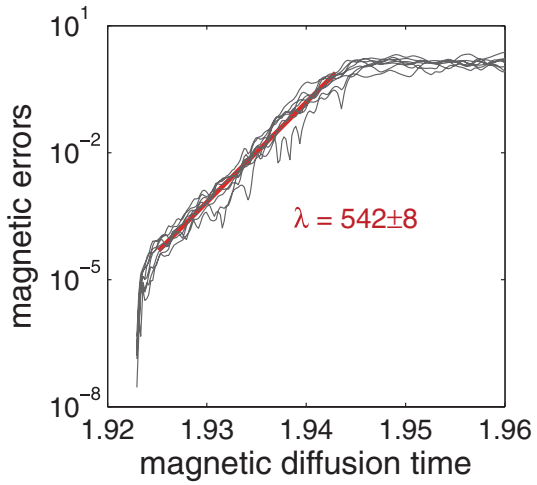

Figure 9. Impact of limited temporal resolution in dynamo B4 as illustrated by the growth of the magnetic errors Δy_n for $n = 1$ to 8 between one solution with a fixed time-step of 10^{-8} τ_η and another one with a fixed time-step of 10^{-6} τ_η. The growth rate (in units of τ_η^{-1}) was estimated with its uncertainty at 95 per cent confidence level.

on Pm. This then leads us to conclude that as a general rule, λ is indeed proportional to U_0/D, but with a factor of proportionality that depends on both E and Pm, that is on the two diffusivities η and ν.

4.2 Comparing the growth rate to the secular-variation timescale

The sensitivity to E of the factor linking λ to U_0/D was already recognised in Hulot *et al.* (2010b). This led to the suggestion that scaling λ with respect to some directly observable dynamo output parameter displaying a similar dependence with respect to U_0/D, could perhaps lead to a clearer picture of what exactly governs the growth rate of the errors, particularly in view of inferring an estimate of $\tau_e = \lambda^{-1}$ for the Earth's dynamo. The candidate parameter was the so-called secular-variation timescale τ_{SV} introduced by Christensen & Tilgner (2004) and recently discussed in Lhuillier *et al.* (2011).

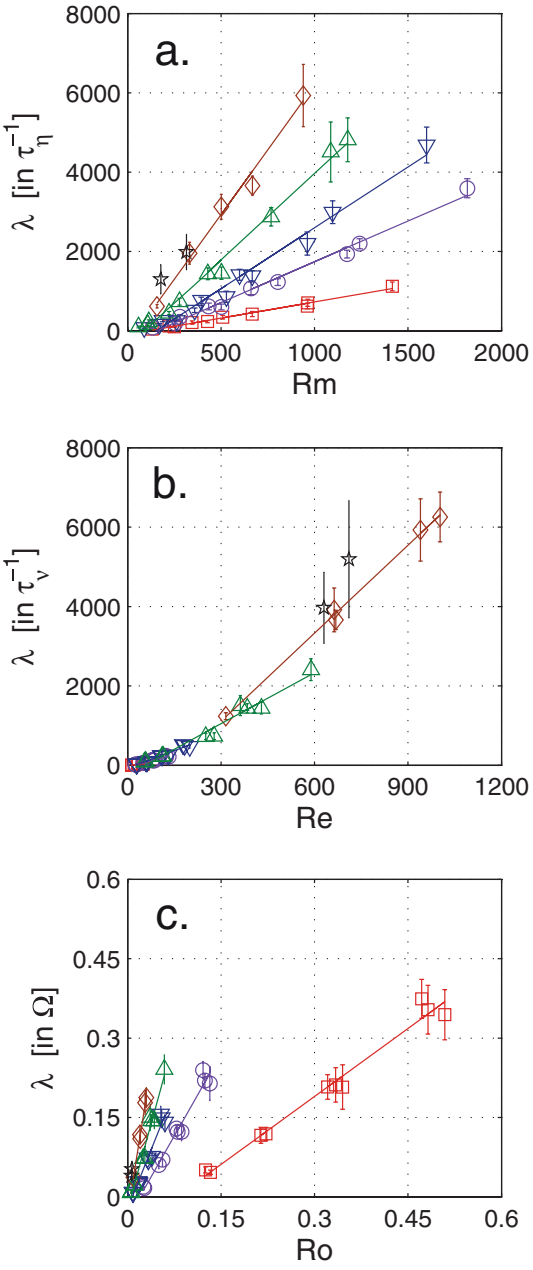

Figure 10. Growth rate λ as a function of Rm (a), Re (b) and Ro (c). Note that λ is counted in units of τ_η^{-1} in (a) (which amounts to plotting $\lambda\tau_\eta$), in units of τ_ν^{-1} in (b) (which amounts to plotting $\lambda\tau_\nu$), and in units of Ω in (c) (which amounts to plotting $\lambda\Omega^{-1}$). Colour codes and symbols refer to E, with $E = 1 \times 10^{-2}$ being shown as red squares, $E = 1 \times 10^{-3}$ as purple circles, $E = 3 \times 10^{-4}$ as blue down-pointing triangles, $E = 1 \times 10^{-4}$ as green up-pointing triangles, $E = 3 \times 10^{-5}$ as brown diamonds, and $E = 1 \times 10^{-5}$ as black stars (error bars refer to 95 per cent level of confidence).

This timescale characterises the time variations of each non-dipole spherical harmonic degree n of the (observable) poloidal field at the core surface, through the relationship:

$$\tau_n = \tau_{SV}/n \quad (n \geqslant 2), \tag{14}$$

where τ_n is the reorganization (or correlation) time introduced by Hulot & Le Mouël (1994) and defined as

$$\tau_n = \sqrt{\frac{\langle \sum_{m=0}^{n} \left[(g_n^m)^2 + (h_n^m)^2 \right] \rangle}{\langle \sum_{m=0}^{n} \left[(\dot{g}_n^m)^2 + (\dot{h}_n^m)^2 \right] \rangle}}, \tag{15}$$

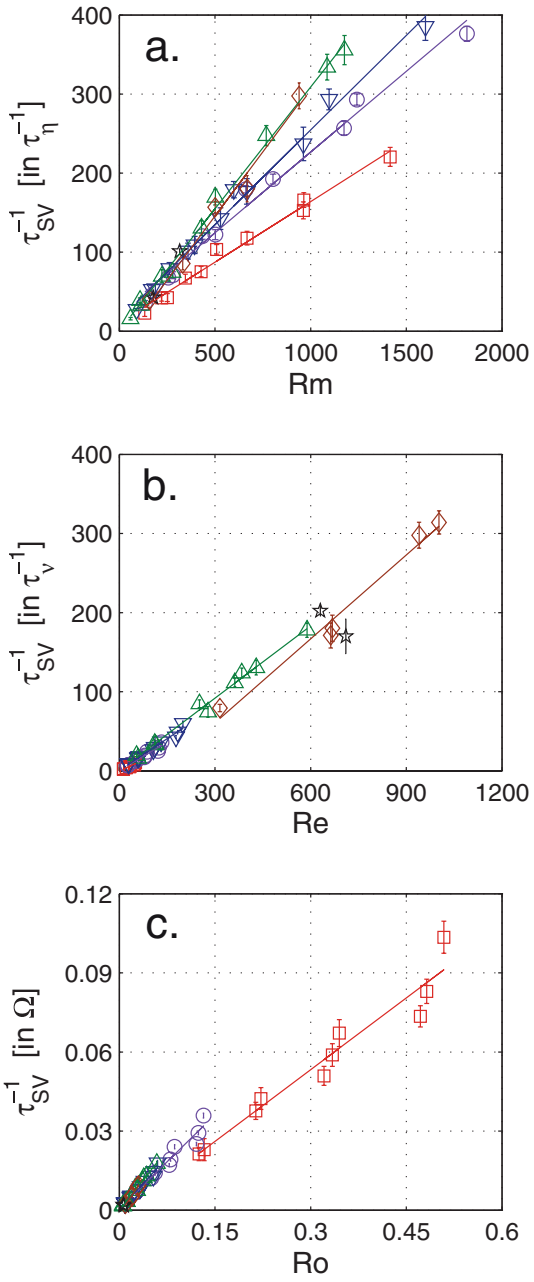

Figure 11. Inverse τ_{SV}^{-1} of the secular-variation timescale as a function of Rm (a), Re (b) and Ro (c). Note that τ_{SV}^{-1} is counted in units of τ_η^{-1} in (a) (which amounts to plotting τ_η/τ_{SV}), in units of τ_ν^{-1} in (b) (which amounts to plotting τ_ν/τ_{SV}), and in units of Ω in (c) (which amounts to plotting $(\tau_{SV}\,\Omega)^{-1}$). Note also that in panel (a), eq. (16) predicts a linear plot ($\tau_\eta/\tau_{SV} = 0.296$ Rm, not shown) indistinguishable from the overlapping linear best fits obtained for E between 10^{-5} and 10^{-4}. Colour codes and symbols refer to E as in Fig. 10 (error bars refer to 95 per cent level of confidence).

where g and h define the Gauss coefficients of the poloidal field at the core surface, $\dot{g}$ and $\dot{h}$ their time derivatives, and the angle brackets refer to time averaging.

In the same way as for λ, it is expected that τ_{SV}^{-1} is proportional to U_0/D. This can be tested using the same three scaling options as was done for λ: plotting $\tau_{SV}^{-1}\,\tau_\eta$ as a function of Rm (Fig. 11a), $\tau_{SV}^{-1}\,\tau_\nu$ as a function of Re (Fig. 11b), and $\tau_{SV}^{-1}\,\Omega^{-1}$ as a function of Ro (Fig. 11c). These plots show that τ_{SV}^{-1} in these dynamo models is close to being proportional to U_0/D, with significantly less dependence on E and

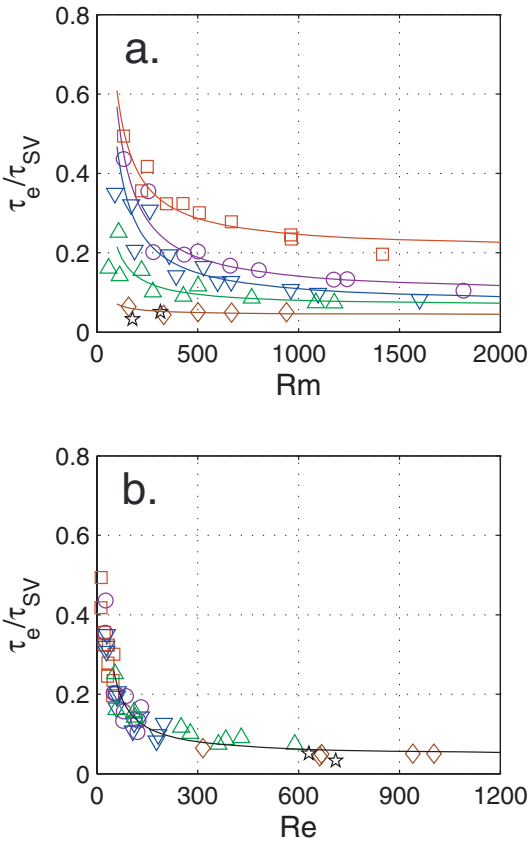

Figure 12. Ratio of the e-folding time τ_e to the secular-variation timescale τ_{SV} as a function of the magnetic Reynolds number Rm (a) and Reynolds number Re (b). Simple fits of the form $\tau_e/\tau_{SV} = a + b/\mathrm{Rm}$ are presented for each value of the Ekman number E (save for $E = 1 \times 10^{-5}$ in view of the scarcity of the values) in panel (a) and a similar fit of the form $\tau_e/\tau_{SV} = a + b/\mathrm{Rm}$ (for all the values) is shown in panel (b). This last best fit leads to an asymptotic estimate of 0.05 ± 0.02 for τ_e/τ_{SV}. Colour codes and symbols refer to E as in Fig. 10.

Pm (and thus on the two diffusivities η and ν) than λ. This behaviour was already noted by Christensen & Tilgner (2004) who proposed that (their fig. 3b, where we correct for our different definitions of τ_η and Rm)

$$\tau_{SV}/\tau_\eta = 3.38\mathrm{Rm}^{-1}. \quad (16)$$

This relationship is indeed compatible with our own results, when considering low enough Ekman numbers (Fig. 11a). Note however that some dependence on E and Pm is still to be found, but mainly for dynamos with high Ekman numbers.

The fact that both λ and τ_{SV}^{-1} are mainly proportional to U_0/D leads us to test the behaviour of $\tau_e = \lambda^{-1}$ rescaled in units of τ_{SV}, which amounts to plotting the non-dimensional quantity τ_e/τ_{SV} as a function of some parameter characterising U_0/D. Again, three options are possible, depending on which timescale we use to measure U_0/D.

We first discuss Fig. 12(a), which shows τ_e/τ_{SV} as a function of Rm. For any fixed Ekman number E, and when Rm increases, τ_e/τ_{SV} progressively decreases towards some asymptotic value, this asymptotic value being reached more rapidly when the Ekman number becomes smaller. Of the order of 0.05 for the lowest Ekman number, this value provides an upper estimate of τ_e/τ_{SV} for dynamos with lower Ekman number, such as the geodynamo.

Interesting additional insight is provided by Fig. 12(b), which shows τ_e/τ_{SV} as a function of Re. This figure reveals a more striking trend for all dynamos we investigated to have τ_e/τ_{SV} converging towards a common value 0.05 ± 0.02 when Re increases. Because only modest variability was considered for Pm for each value of the Ekman number, plotting τ_e/τ_{SV} as a function of Re in place of Rm essentially amounts to rescaling each curve of Fig. 12(a) according to Pm, to produce the single curve in Fig. 12(b). It can then be interpreted as an indication that all curves with fixed Ekman numbers in Fig. 12(a) tend to eventually converge towards the common value of 0.05 ± 0.02 when Rm becomes large enough.

Our results thus suggest that the two diffusivities η and ν are important parameters, and that the asymptotic value of 0.05 ± 0.02 we found for τ_e/τ_{SV} is only reached provided that E is small enough, whereas both Rm and Re are large enough.

4.3 Comparing the growth rate to the dissipation times

The previous analysis raises the intriguing question of the origin of the asymptotic value we found for τ_e/τ_{SV}. This value is significantly different from order 1, and one may wonder why such a small ratio is obtained. Interestingly, a comparable ratio is found between the magnetic dissipation time τ_{diss}^{mag} introduced by Christensen & Tilgner (2004) and τ_{SV}, possibly suggesting a more fundamental link between τ_e and τ_{diss}^{mag} than between τ_e and τ_{SV}.

This magnetic dissipation time is defined as the ratio $\tau_{diss}^{mag} = E_{mag}/D_{Ohm}$ of the total magnetic energy of the dynamo

$$E_{mag} = \frac{1}{2\mu_0}\int \boldsymbol{B}_0^2 \mathrm{d}V \tag{17}$$

to the total Ohmic dissipation power

$$D_{Ohm} = \frac{\eta}{\mu_0}\int (\boldsymbol{\nabla}\times\boldsymbol{B}_0)^2 \mathrm{d}V, \tag{18}$$

where the integrals are computed over the volume of the dynamo shell. Just like τ_{SV}, τ_{diss}^{mag} can be expected to scale like Rm^{-1} when measured in units of τ_η. To see this, it is important to first recognise that because the dynamo is in a saturated regime, eq. (10) implies that on average D_{Ohm} also satisfies

$$D_{Ohm} = \frac{1}{2\mu_0}\int \boldsymbol{B}_0\cdot\boldsymbol{\nabla}\times(\boldsymbol{u}_0\times\boldsymbol{B}_0)\mathrm{d}V. \tag{19}$$

It is then quite natural to expect D_{Ohm} to scale as $B_0^2 U_0 V/(\mu_0 D)$, where V is the volume of the dynamo shell. Similarly, it is natural to expect E_{mag} (as given by eq. 17) to scale as $B_0^2 V/\mu_0$. This then leads to the suggestion that $\tau_{diss}^{mag} = E_{mag}/D_{Ohm}$ scales like $D/U_0 = \tau_\eta\,\mathrm{Rm}^{-1}$. Christensen & Tilgner (2004) already found that τ_{diss}^{mag} is essentially proportional to Rm^{-1} when counted in units of τ_η (for dynamo simulations with E ranging from 1×10^{-5} to 3×10^{-4}, when using our definition of E, see their fig. 1a). This led them to propose that $\tau_{diss}^{mag}/\tau_\eta = 0.27\ \mathrm{Rm}^{-1}$ (their eq. 3, which we modify for our definitions of τ_η and Rm). Such a relationship implies that $(\tau_{diss}^{mag})^{-1}$ plots as a linear function of Rm when scaled in units of τ_η^{-1}. Fig. 13 shows that this is indeed the case for the simulations we ran. But as was already observed for both λ (Fig. 10a) and τ_{SV}^{-1} (Fig. 11a), some dependence on E is also to be found for the slope. Interestingly, just like for τ_{SV}^{-1}, this dependence weakens as E decreases. Searching for a best linear fit for the simulations with the smallest Ekman numbers we ran (between $E = 1\times10^{-5}$ and $E = 1\times10^{-4}$) then leads to

$$\tau_{diss}^{mag}/\tau_\eta = 0.18(\pm0.02)\mathrm{Rm}^{-1}. \tag{20}$$

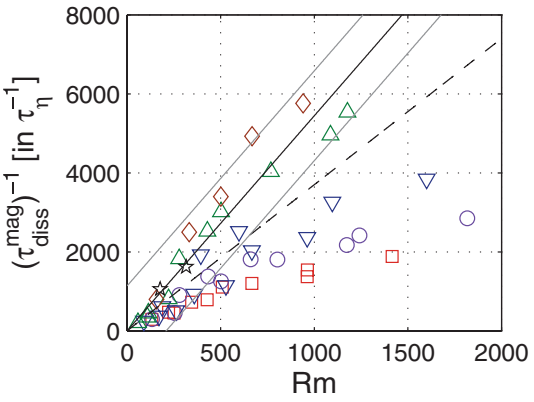

Figure 13. $(\tau_{diss}^{mag})^{-1}$ counted in units of τ_η^{-1} (which amounts to plotting $\tau_\eta/\tau_{diss}^{mag}$) as a function of Rm. Also shown, the scaling suggested by Christensen & Tilgner (2004) (dashed line), and our best fit to values corresponding to E between 1×10^{-5} and 1×10^{-4}, leading to eq. (20) (solid line, with light lines referring to 95 per cent level of confidence). Colour codes and symbols refer to E as in Fig. 10.

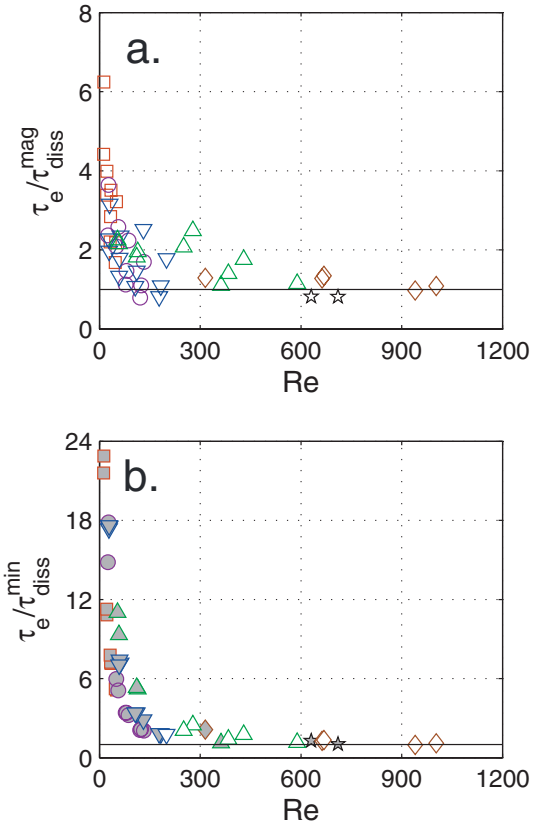

Figure 14. Ratio of the e-folding time τ_e to the magnetic dissipation time τ_{diss}^{mag} (a) and to the minimum min $(\tau_{diss}^{kin}, \tau_{diss}^{mag})$ of the viscous and magnetic dissipation times (b) as a function of Re. Colour codes and symbols refer to E as in Fig. 10. In panel (b), grey-filled symbols indicate values obtained when $\tau_{diss}^{kin} < \tau_{diss}^{mag}$.

Combined together, eqs (20) and (16) lead to a ratio $\tau_{diss}^{mag}/\tau_{SV}$ of the order of 0.05, identical to the asymptotic value we found for τ_e/τ_{SV}. These considerations prompted us to directly investigate the behaviour of τ_e/τ_{diss}^{mag} as a function of Re, for comparison with Fig. 12(b). As can be seen in Fig. 14(a), it now appears that τ_e/τ_{diss}^{mag}

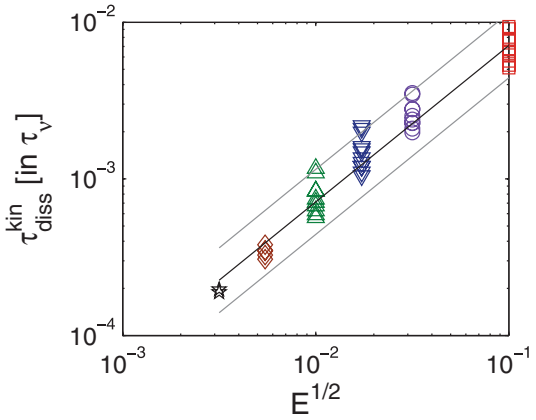

Figure 15. τ^{kin}_{diss} counted in units of τ_ν (which amounts to plotting $\tau^{kin}_{diss}/\tau_\nu$) as a function of $E^{1/2}$. Also shown our best fit leading to eq. (23) (solid line, with light lines referring to 95 per cent level of confidence). Colour codes and symbols refer to E as in Fig. 10.

converges towards unity as both E decreases and Re increases. This then suggests that for dynamos with low E and high Re and Rm, τ_e is governed by the magnetic dissipation time τ^{mag}_{diss}. Because $(\tau^{mag}_{diss})^{-1}$ reflects the rate at which magnetic energy is both lost and supplied in the dynamo (because the field is permanently maintained), this then leads us to suggest that for low enough E and high enough Re and Rm, what ultimately governs the growth rate $\lambda = \tau_e^{-1}$ is the rate with which magnetic energy can be provided by the system to feed the error growth.

At this point however, it is important to recall that the error growth not only affects the magnetic field but also the other fields, and that the rate at which kinetic energy is provided to compensate for viscous dissipation could therefore also play a role. This rate can be measured via an analogous viscous dissipation time defined as the ratio $\tau^{kin}_{diss} = E_{kin}/D_{vis}$ of the total kinetic energy of the dynamo

$$E_{kin} = \frac{\rho_0}{2}\int \boldsymbol{u}_0^2 \mathrm{d}V \tag{21}$$

to the total viscous dissipation power

$$D_{vis} = \rho_0 \nu \int (\boldsymbol{\nabla}\times\boldsymbol{u}_0)^2 \mathrm{d}V, \tag{22}$$

where the integrals are computed over the dynamo shell.

Interestingly, this second dissipation time τ^{kin}_{diss} scales very differently. Although the formal analogy of eqs (17) and (21) on the one hand, and (18) and (22) on the other hand, would suggest that τ^{mag}_{diss} is simply related to τ^{kin}_{diss} via a factor $Pm = \nu/\eta$, this turns out not to be the case. The reason for this is that the detailed way the dissipation occurs is very different for D_{Ohm} and D_{vis}. To properly scale D_{vis}, we must recognise that most of the viscous dissipation occurs within the Ekman boundary layer, of thickness δ scaling as $(\nu/\Omega)^{1/2}$. This then leads D_{vis} (as given by eq. 22) to scale as $\rho_0 \nu\, U_0^2\, S/\delta$, where S is the outer surface of the shell, while E_{kin} (as given by 21) scales as $\rho_0\, U_0^2\, V$. This in turn implies that $\tau^{kin}_{diss} = E_{kin}/D_{vis}$ scales as $D\delta/\nu = D/(\nu\Omega) = \Omega^{-1}\, E^{-1/2} = \tau_\nu\, E^{1/2}$. As can be seen in Fig. 15, τ^{kin}_{diss} essentially scales as $E^{1/2}$ when measured in units of τ_ν for all the dynamos we considered, with a best fit leading to

$$\tau^{kin}_{diss}/\tau_\nu = 0.071(\pm 0.004)E^{1/2}. \tag{23}$$

This equation, together with eq. (20), then makes it possible to identify which of τ^{kin}_{diss} and τ^{mag}_{diss} is the shortest for a given dynamo. These equations can indeed be combined so that the ratio $\tau^{kin}_{diss}/\tau^{mag}_{diss}$ can directly be expressed as

$$\tau^{kin}_{diss}/\tau^{mag}_{diss} = 0.39(\pm 0.07)ReE^{1/2}. \tag{24}$$

This being established, we now note that all our simulations with low Re (less than typically 200) happen to display a τ^{kin}_{diss} smaller than τ^{mag}_{diss} [as can be seen in Fig. 14(b), where we plot τ_e/min $(\tau^{kin}_{diss}, \tau^{mag}_{diss})$ as a function of Re]. This suggests that viscosity could also play a significant role in controlling the rate of error growth for these dynamos. However, for most of our simulations with high Re (above typically 200), τ^{kin}_{diss} was found to be larger than τ^{mag}_{diss}, and this suggests that for these dynamos, viscous dissipation plays a minor role compared to magnetic dissipation. This is consistent with the fact that τ_e asymptotically equates to τ^{mag}_{diss} for those high Re simulations. Nevertheless, we note that in the few instances when τ^{kin}_{diss} was found to be (then slightly) smaller than τ^{mag}_{diss} for such high Re, τ_e happens to be closer to τ^{kin}_{diss} than to τ^{mag}_{diss} (Fig. 14b).

From these results, we suggest that for low enough E and high enough Re and Rm, provided that τ^{kin}_{diss} is larger than τ^{mag}_{diss} (as can be assessed thanks to eq. 24), what governs the error growth in a dynamo, is the rate $(\tau^{mag}_{diss})^{-1}$ with which magnetic energy can be provided to feed the growth of the errors.

5 SUMMARY OF RESULTS

In this study we investigated, both from a numerical and a theoretical point of view, the growth of errors initially introduced in numerical dynamo simulations. As was shown in Section 3, one of the most remarkable properties of this error growth is its universal and robust character. Irrespective of the type, the amplitude and the time of the perturbation introduced, it always resulted in an exponential error growth. Furthermore, for any fixed dynamo regime defined by a set of non-dimensional parameters Ra^*, E, Pr and Pm, this rate was always found to be the same, to within little variability. The largest cause of variability was found to be related to the time of the perturbation introduced, causing an approximately normal distribution of the recovered rates, with a standard deviation of the order of 6 per cent of the mean rate. When considering random perturbations introduced at a given fixed time, this standard deviation was found to be lower, of the order of 3 per cent. The only exception to this general rule was found when the amplitude of the perturbation introduced was very large (typically greater than 10^{-2}), in which case the growth rate was found to slightly slows. Similar slowing was observed by meteorologists when they carried out similar analysis of the atmospheric system (e.g. Smagorinsky 1969). But it is worth noting that, in contrast to what we observed for dynamos, these meteorological studies reveal much more sensitivity of the error growth to the details of the instantaneous atmospheric state (e.g. Charney *et al.* 1966; Kalnay 2003, for more recent illustrations).

Thanks to its universal and robust character, the growth rate was estimated for a large set of control parameters, and scaling laws were sought to investigate the cause of the error growth. Based on an analysis of eqs (8)–(10) governing the reference solution and of eqs (11)–(13) governing the perturbation, we argued that the growth rate λ was mainly proportional to U_0/D (Section 4.1), as had originally been proposed in Hulot *et al.* (2010b). We also observed (Fig. 10) that the factor of proportionality linking λ to U_0/D depended on E and Pm (Pr being anyway set to 1 in all our simulations). But rather than making an attempt to scale λ also with respect to E and Pm, we investigated the possibility of directly scaling the e-folding time $\tau_e = \lambda^{-1}$ of the error growth with respect to other relevant dynamo output timescales. Three such timescales were identified,

the secular-variation timescale τ_{SV} defined by eqs (14) and (15), the magnetic dissipation time τ_{diss}^{mag} defined by eqs (17) and (18) and the kinetic dissipation time τ_{diss}^{kin} defined by eqs (21) and (22).

Scaling τ_e with respect to τ_{SV}, we found that some asymptotic value of 0.05 ± 0.02 was eventually reached for τ_e/τ_{SV}, provided that E was small enough, while both Rm and Re were large enough (Section 4.2). Scaling τ_e with respect to τ_{diss}^{mag} led to further insight. We showed that $(\tau_{diss}^{mag})^{-1}$ was also primarily proportional to U_0/D (Section 4.3). Guided by Christensen & Tilgner (2004) who had investigated the behaviour of both $\tau_{diss}^{mag}/\tau_\eta$ and τ_{SV}/τ_η as a function of Rm, we noted that a value of 0.05 was found for the ratio $\tau_{diss}^{mag}/\tau_{SV}$, when E was small enough. The coincidence between the value of 0.05 found for $\tau_{diss}^{mag}/\tau_{SV}$, and the asymptotic value of 0.05 ± 0.2 previously found for τ_e/τ_{SV}, was a clear incentive to more closely investigate the behaviour of τ_e/τ_{diss}^{mag}. Plotting τ_e/τ_{diss}^{mag} as a function of Re revealed that this ratio tended to reach an asymptotic value of unity when Re became large enough (Fig. 14a). This was interpreted as the fact that the growth rate of the errors could be controlled by the rate with which magnetic energy could be provided by the flow to feed the error growth. But we also noted that kinetic energy, just like magnetic energy, could also contribute. The rate at which kinetic energy could be provided being characterised by τ_{diss}^{kin}, we also investigated the behaviour of this quantity, which scales very differently from τ_{diss}^{mag} (eq. 23). We noted that for most of our simulations with low Re, this timescale was shorter than τ_{diss}^{mag}, implying a significant role of viscosity in controlling the growth rate for such dynamos. But we also noted that most of our simulations with high Re had τ_{diss}^{kin} larger than τ_{diss}^{mag}, confirming the leading role of this timescale in controlling the error growth for these dynamos.

Taken together, our results suggest that τ_e is controlled by τ_{diss}^{mag} as soon as dynamos with low enough E, and large enough Re and Rm are considered, and provided that $\tau_{diss}^{kin}/\tau_{diss}^{mag}$ is large enough (as can be assessed with the help of eq. 24). As we shall see next, the geodynamo is one such dynamo. We therefore propose that the growth rate of the errors for the geodynamo could be identical to its τ_{diss}^{mag} magnetic dissipation time.

6 IMPLICATIONS FOR THE EARTH'S DYNAMO LIMIT OF PREDICTABILITY

Hulot *et al.* (2010b) noted that τ_e/τ_{SV} tended to converge towards a value of 0.05 as soon as E was small enough and Rm large enough. This result was then used to infer an empirical value $\tau_e \approx 30$ yr for the geodynamo, assuming $\tau_{SV} = 535$ yr, as proposed by Christensen & Tilgner (2004). The authors were however unaware of what could be responsible for the asymptotic value $\tau_e/\tau_{SV} = 0.05$, and it is important that we now reconsider these earlier results in view of the present more extensive study.

Taking $D \approx 2260$ km and $\eta = 1.32$ m^2 s^{-1}, we first estimate $\tau_\eta \approx 120$ kyr for the Earth's core. We next assume $\tau_{SV} = 535$ yr for the Earth's magnetic field (Christensen & Tilgner 2004) and rely on eq. (16) to estimate Rm ≈ 760. Because Re = Rm/Pm, this then implies that Re is at least of the order of 7×10^7 (assuming a standard value of Pm $= 10^{-5}$). Further noting that for the Earth's core the Ekman number locates in the range E $= 10^{-15}$–10^{-14} (Christensen & Wicht 2007), this shows that the geodynamo is well in the regime we identified in this study, such that τ_e would equate to τ_{diss}^{mag}, provided that τ_{diss}^{mag} is smaller than τ_{diss}^{kin}.

To assess whether this last condition is met for the geodynamo, we use Rm ≈ 760 and rely on eq. (20) to estimate $\tau_{diss}^{mag} \approx 30$ yr. Taking E $= 10^{-15}$–10^{-14}, we next rely on eq. (23)—which we slightly recast into the equivalent formulation $\tau_{diss}^{kin} = 0.07\Omega^{-1}\,\mathrm{E}^{-1/2}$—to infer $\tau_{diss}^{kin} = 310$–980 yr. Comparing these estimates of τ_{diss}^{mag} and τ_{diss}^{kin} shows that τ_{diss}^{mag} is indeed smaller than τ_{diss}^{kin} for the geodynamo, by at least one order of magnitude. We thus propose that τ_e is governed by τ_{diss}^{mag} to which it can be identified. This in turn leads us to estimate $\tau_e \approx 30$ yr, leading to an error doubling time of $\ln(2) \cdot \tau_e \approx 21$ yr.

It is not fortuitous that the same value $\tau_e \approx 30$ yr is reached here as in Hulot *et al.* (2010b). It simply reflects the fact that the empirical result $\tau_e/\tau_{SV} = 0.05$ is a direct consequence of both τ_{SV} and τ_{diss}^{mag} scaling as Rm when counted in units of τ_η to within precisely that factor (recall eqs 16 and 20). In contrast, our estimate of τ_e is now directly based on our contention that τ_e is governed by τ_{diss}^{mag}.

Now what about the practical limit of predictability of the geodynamo? Inferring this limit not only requires an estimate of τ_e. It also requires some knowledge of how well the dynamical state of the geodynamo is known at some initial time. If this initial imperfect knowledge can be cast in the form of some relative error of amplitude ε in any of the magnetic, flow or temperature field, our results of Section 3 show that this error would be quickly communicated to all other dynamo fields and next grow exponentially with the rate defined by τ_e, so that the effective limit of predictability would be of the order of $\Delta t = \ln\left(\varepsilon^{-1}\right)\tau_e$.

In practice, the situation is however more complex. Despite recent progress in satellite measurements (e.g. Gillet *et al.* 2010), only the largest scales of the radial field at the core surface can directly be recovered (e.g. Hulot *et al.* 2007) because the smallest scales are concealed by the lithospheric field (e.g. Hulot *et al.* 2009). This limitation is however mitigated by the fact that the field at the core surface can be reconstructed far back in time (e.g. Hulot *et al.* 2010a). Historical models (e.g. Jackson *et al.* 2000) and archaeomagnetic models (e.g. Korte & Constable 2005) provide useful information over centennial and millennial timescales, and could be used in the context of data assimilation to produce an estimate of the current dynamical state of the geodynamo (e.g. Fournier *et al.* 2010).

Were dynamo simulations employed to produce forecasts of the magnetic field, the practical limit of predictability would be defined by both the value $\tau_e \approx 30$ yr and all the combined sources of errors with which the initial state of the geodynamo could be approximated, but also by further errors introduced by the necessarily limited resolution of the numerical model. We saw in Section 3.3 that the impact of such a limited resolution was quite comparable to that of an additional initial relative error of ε', the main cause of this error being due to spatial rather than temporal resolution. We suggested a simple way of assessing the magnitude of this equivalent initial error, which can be kept reasonably low if enough numerical resolution is achieved, but we saw can hardly be less than $\varepsilon' = 10^{-3}$.

Finally, it is important to recall that all numerical models are unfortunately forced to run in parameter regimes that are still very far from that of the true geodynamo, so that none can yet claim to be completely appropriate. Although progress in computational resources will certainly help improve on this situation, and our study or that of Christensen *et al.* (2010) could be used to assist in the best choice of workable parameters, this will inevitably result in some additional unknown error, and further reduce the practical limit of predictability. Unfortunately and despite some interesting suggestions (Liu *et al.* 2007), there is no simple way of anticipating how severe the effect of this unknown error could be.

Hulot *et al.* (2010b) previously noted that satellite data currently make it possible to build field models that correctly describe the core

field at the Earth's surface to within 10–20 nT (which is mainly the effect of ignoring the unknown small scales of this core field), and that simple linear temporal extrapolation of this field usually leads to an error roughly 10 times larger after 5 years (e.g. Maus *et al.* 2008). Estimating $\tau_e \approx 30$ yr, they concluded that, in the best of all worlds and with the help of an optimised data-assimilation scheme, a similar increase in error might be achieved after roughly ln (10) $\tau_e = 70$ yr. This estimate ignored that very little is known about the dynamical state of the geodynamo beyond the observable field it produces, and it only took the impact of ignoring the small scales of the observed field into account in a very optimistic way. Assessing the true limit of predictability of data-assimilation schemes will clearly require much more work, and will probably have to wait for the advent of the first operational such codes. Nevertheless, it is clear that the value of 30 yr we estimate for τ_e, is a very serious challenge in view of the many sources of errors that can grow exponentially at that pace.

ACKNOWLEDGMENTS

We thank Andrew Tangborn and an anonymous reviewer for their very constructive reviews. This study was supported by the SEDIT programme of CNRS-INSU. Numerical computations were performed at S-CAPAD, IPGP, France and at HPC resources from GENCI-CINES/IDRIS (Grant 2009-042122 and 2010-042122). This is IPGP contribution 3139.

REFERENCES

Aubert, J., Aurnou, J.M. & Wicht, J., 2008. The magnetic structure of convection-driven numerical dynamos, *Geophys. J. Int.,* **172**(3), 945–956, doi: 10.1111/j.1365-246X.2007.03693.x.

Beggan, C.D. & Whaler, K.A., 2009. Forecasting change of the magnetic field using core surface flows and ensemble Kalman filtering, *Geophys. Res. Lett.,* **36**, L18303, doi: 10.1029/2009GL039927.

Charney, J., Fleagle, R., Riehl, H., Lally, V. & Wark, D., 1966. The feasibility of a global observation and analysis experiment, *Bull. Am. Meteorol. Soc.,* **47**, 200–220.

Christensen, U.R. & Aubert, J., 2006. Scaling properties of convection-driven dynamos in rotating spherical shells and application to planetary magnetic fields, *Geophys. J. Int.,* **166**(1), 97–114, doi: 10.1111/j.1365-246X.2006.03009.x.

Christensen, U.R. & Tilgner, A., 2004. Power requirement of the geodynamo from ohmic losses in numerical and laboratory dynamos, *Nature,* **429**(6988), 169–171, doi: 10.1038/nature02508.

Christensen, U.R. & Wicht, J., 2007. Numerical Dynamo Simulations, in *Core Dynamics, Vol. 8 of Treatise on Geophysics*, pp. 245–281, eds Olson, P. & Schubert, G., Elsevier, Amsterdam.

Christensen, U.R., Olson, P.L. & Glatzmaier, G., 1999. Numerical modelling of the geodynamo: a systematic parameter study, *Geophys. J. Int.,* **138**(2), 393–409, doi: 10.1046/j.1365-246X.1999.00886.x.

Christensen, U.R. *et al.*, 2001. A numerical dynamo benchmark, *Phys. Earth planet. Inter.,* **128**(1–4), 25–34, doi: 10.1016/S0031-9201(01)00275-8.

Christensen, U.R., Aubert, J. & Hulot, G., 2010. Conditions for Earth-like geodynamo models, *Earth planet. Sci. Lett.,* **296**(3-4), 487–496, doi: 10.1016/j.epsl.2010.06.009.

Finlay, C.C. *et al.*, 2010. International geomagnetic reference field: the eleventh generation, *Geophys. J. Int.,* **183**(3), 1216–1230, doi: 10.1111/j.1365-246X.2010.04804.x.

Fournier, A., Eymin, C. & Alboussière, T., 2007. A case for variational geomagnetic data assimilation: insights from a one-dimensional, nonlinear, and sparsely observed MHD system, *Nonlinear Process. Geophys.,* **14**(2), 163–180, doi: 10.5194/npg-14-163-2007.

Fournier, A. *et al.*, 2010. An introduction to data assimilation and predictability in geomagnetism, *Space Sci. Rev.,* **155**, 247–291, doi: 10.1007/s11214-010-9669-4.

Friis-Christensen, E., Lühr, H. & Hulot, G., 2006. Swarm: a constellation to study the Earth's magnetic field, *Earth Planets Space,* **58**(4), 351–358.

Gillet, N., Lesur, V. & Olsen, N., 2010. Geomagnetic core field secular variation models, *Space Sci. Rev.,* **155**, 129–145, doi: 10.1007/s11214-009-9586-6.

Glatzmaier, G. & Roberts, P.H., 1995a. A three-dimensional convective dynamo solution with rotating and finitely conducting inner core and mantle, *Phys. Earth planet. Inter.,* **91**(1–3), 63–75, doi: 10.1016/0031-9201(95)03049-3.

Glatzmaier, G. & Roberts, P.H., 1995b. A three-dimensional self-consistent computer-simulation of a geomagnetic-field reversal, *Nature,* **377**(6546), 203–209, doi: 10.1038/377203a0.

Hulot, G. & Le Mouël, J.-L., 1994. A statistical approach to the Earth's main magnetic field, *Phys. Earth planet. Inter.,* **82**(3–4), 167–183, doi: 10.1016/0031-9201(94)90070-1.

Hulot, G., Olsen, N. & Sabaka, T., 2007. The present field, in *Geomagnetism, Vol.5 of Treatise on Geophysics*, pp. 33–75, ed. Kono, M., Elsevier, Amsterdam.

Hulot, G., Olsen, N., Thébault, E. & Hemant, K., 2009. Crustal concealing of small-scale core-field secular variation, *Geophys. J. Int.,* **177**(2), 361–366, doi: 10.1111/j.1365-246X.2009.04119.x.

Hulot, G., Finlay, C.C., Constable, C.G., Olsen, N. & Mandea, M., 2010a. The magnetic field of planet Earth, *Space Sci. Rev.,* **152**, 159–222, doi: 10.1007/s11214-010-9644-0.

Hulot, G., Lhuillier, F. & Aubert, J., 2010b. Earth's dynamo limit of predictability, *Geophys. Res. Lett.,* **37**, L06305, doi: 10.1029/2009GL041869.

Jackson, A., Jonkers, A.R.T. & Walker, M.R., 2000. Four centuries of geomagnetic secular variation from historical records, *Philos. Trans. R. Soc. Lond., A,* **358**(1768), 957–990, doi: 10.1098/rsta.2000.0569.

Kageyama, A., Sato, T., Horiuchi, R., Hayashi, T., Todo, Y., Watanabe, T. & Takamaru, H., 1995. Computer-simulation of a magnetohydrodynamic dynamo. II, *Phys. Plasmas,* **2**(5), 1421–1431, doi: 10.1063/1.871485.

Kalnay, E., 2003. Atmospheric predictability and ensemble forecasting, in *Atmospheric Modeling, Data Assimilation and Predictability*, pp. 205–260, Cambridge University Press, Cambridge.

Korte, M. & Constable, C.G., 2005. Continuous geomagnetic field models for the past 7 millennia: 2. CALS7K, *Geochem. Geophys. Geosyst.,* **6**, Q02H16, doi: 10.1029/2004GC000801.

Kuang, W., Tangborn, A., Jiang, W., Liu, D., Sun, Z., Bloxham, J. & Wei, Z., 2008. MoSST_DAS: the first generation geomagnetic data assimilation framework, *Commun. Comput. Phys.,* **3**(1), 85–108.

Kutzner, C. & Christensen, U.R., 2002. From stable dipolar towards reversing numerical dynamos, *Phys. Earth planet. Inter.,* **131**(1), 29–45, doi: 10.1016/S0031-9201(02)00016-X.

Leith, C., 1965. Numerical simulation of the Earth's atmosphere, in *Methods in Computational Physics,* vol. 4, pp. 1–28, Academic Press, New York, NY.

Lhuillier, F., Fournier, A., Hulot, G. & Aubert, J., 2011. The geomagnetic secular-variation timescale in observations and numerical dynamo models, *Geophys. Res. Lett.*, **38,** L09306, doi:10.1029/2011GL047356.

Liu, D., Tangborn, A. & Kuang, W., 2007. Observing system simulation experiments in geomagnetic data assimilation, *J. geophys. Res.,* **112**(B8), doi: 10.1029/2006JB004691.

Lorenz, E., 1963a. Predictability of hydrodynamic flow, *Trans. New York Acad. Sci.,* **25**(4), 409–432.

Lorenz, E., 1963b. Deterministic nonperiodic flow, *J. Atmos. Sci.,* **20**(2), 130–141.

Lorenz, E., 1965. A study of the predictability of a 28-variable atmospheric model, *Tellus,* **17**(3), 321–333.

Maus, S., Silva, L. & Hulot, G., 2008. Can core-surface flow models be used to improve the forecast of the Earth's main magnetic field?, *J. geophys. Res.,* **113**, B08102, doi: 10.1029/2007JB005199.

Mintz, Y., 1964. Very long-term global integration of the primitive equations of atmospheric motion, in *WMO/IUGG Symposium on Research and*

Development Aspects of Long-Range Forecasting, WMO Technical Note, Vol. 66, pp. 141–167.

Olson, P.L. & Christensen, U.R., 2006. Dipole moment scaling for convection-driven planetary dynamos, *Earth planet. Sci. Lett.,* **250**(3–4), 561–571, doi: 10.1016/j.epsl.2006.08.008.

Silva, L., Maus, S., Hulot, G. & Thébault, E., 2010. On the possibility of extending the IGRF predictive secular model to a higher SH degree, *EPS,* **62**(10), 815–820, doi: 10.5047/eps.2010.07.005.

Simmons, A., Mureau, R. & Petroliagis, T., 1995. Error growth and estimates of predictability from the ECMWF forecasting system, *Q. J. R. Meteorol. Soc.,* **121**, 1739–1771.

Smagorinsky, J., 1963. General circulation experiments with the primitive equations, *Mon. Wea. Rev.,* **91**(3), 99–164.

Smagorinsky, J., 1969. Problems and promises of deterministic extended range forecasting, *Bull. Am. Meteorol. Soc.,* **50**, 286–311.